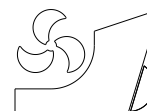


Sabri Alkan<http://dx.doi.org/10.21278/brod73407>ISSN 0007-215X
eISSN 1845-5859

ENHANCEMENT OF MARINE CORROSION AND TRIBOCORROSION RESISTANCE OF OFFSHORE MOORING CHAIN STEEL BY ALUMINIZING PROCESS

UDC 629.5.028.712:621.78.019.84:669.718

Original scientific paper

Summary

The safety of mooring systems and accessories is one of the most critical issues in the structural integrity of floating oil/gas and renewable offshore structures. Mooring chains and accessories operate under dynamic conditions in harsh marine environments. They are subject to severe wear and corrosion between their links due to relative movement from waves, wind, and ocean currents that disrupt structural integrity. To cope with this problem, the pack-aluminizing process was applied on the R4 grade offshore mooring chain steel for 2 h at 850 °C to improve corrosion and wear-corrosion (tribocorrosion) resistance in 3.5% NaCl. The tribocorrosion behaviour of untreated and aluminized samples was investigated by a tribo-electrochemical setup that simultaneously allows for collecting the wear and corrosion data. Potentiodynamic and potentiostatic corrosion and tribocorrosion tests were carried out to understand corrosion kinetics. Optical, SEM, XRD and EDS analyses were performed to characterize the aluminide layer and surface morphologies before and after tribocorrosion investigations. In polarization scans under corrosion and tribocorrosion conditions, the current showed a significant activation stretch of several orders of magnitude, with minor potential changes in the anodic region. Due to the galvanic effects of sliding under natural electrochemical conditions, the untreated R4 alloy exhibited cathodic properties in the wear track, while the aluminium coating was out of the wear track due to its oxide-forming ability. At the cathodic potential, two hard Al₂O₃ materials under pure mechanical effects and third bodies emerging from cracks on the coating surface increase the friction coefficient (COF), while the oxide product film, which has a lubricating ability and pits which reduces the contact area, caused a decrease in COF at the high anodic potential. The study revealed that while the aluminide layer improved the corrosion and tribological character of R4 alloy, material loss from wear track increased due to micro fractures and cracks in the coating layer during sliding tribocorrosion conditions.

Keywords: Offshore; mooring chain; aluminization; corrosive wear; seawater

1. Introduction

The structural integrity of floating structures has become an essential issue in the marine and offshore oil/gas industry in the last century [1–3]. Moreover, the reliability of fixed and floating renewable energy structures, which have emerged as a new field in the last decades, is also significantly discussed [4–11]. One of the most critical issues in the structural integrity of floating offshore structures is the safety of mooring systems and accessories (connectors) [12–15]. Offshore mooring systems are crucial for permanently anchored floating structures in oil/gas and renewable energy applications vulnerable to corrosion-enhanced fatigue damage [16–19]. Mooring chains and accessories are subject to severe wear between links due to relative movement from waves, wind and ocean currents [20,21]. Mooring lines are also exposed to abrasion and impact in the splash zone generated by heavy waves and floating objects and face abrasive effects in the thrash zone [22,23]. Moreover, corrosion is more severe in the splash zone than in other areas due to higher oxygen concentrations for offshore structures and their mooring systems [10,24,25]. Marine corrosion combined with mechanical loading, namely tribocorrosion, is one of the significant causes of mooring chain and accessories damage [19,26–30]. Several incidents occurred between 2001 and 2011 in the mooring systems of floating offshore structures, and malfunctions were caused by 19% wire rope, 54% due to chains and 19% by their accessories (connection equipment) [26]. It has been determined that the damages mainly occur in the form of corrosion (20%), fatigue (17%) and fatigue/corrosion (19%) (caused by wear-corrosion interaction) [31]. Ma et al. studies also emphasized that fatigue and corrosion contribute to 64% of failure events. The data indicate that wear and corrosion degradation of mooring systems plays an essential role in the structural integrity of offshore structures and their mooring systems [8]. Thus, improving the tribocorrosion resistance of the mooring chains and accessories is a vital research topic.

The offshore mooring chains and their accessories (connectors), such as pear links, kenter links, C-links, H-links, shackles and D-shackles, are available to satisfy the high tensile strength demand from 690 MPa to 1000 MPa in various qualities (R3, R3S, R4, R4S and R5) [32]. The classification societies inspect offshore mooring systems for the structure's safety, and unavoidable wear margins are allowed according to the standards [32,33]. Optimizing wear and corrosion margins is an essential structural integrity criterion for marine and ship structures [34]. However, inspection, replacement and maintenance of chains and connectors in offshore mooring systems are complex and costly [9]. The coating systems can reduce the high maintenance and replacement costs of damaged components and prevent the early collapse of floating structures or parts [35,36]. For this purpose, different coatings have been proposed as an essential solution to protect offshore mooring systems from wear and corrosion. In this direction, several researchers have studied to overcome wear, corrosion, and tribocorrosion issues in offshore mooring chains and accessories by surface modifications [37–43].

Since the onset of wear and corrosion corresponds to materials' surface properties, improving only the surface properties rather than the entire material is often a more cost-effective method for resistance to tribocorrosion [44]. Due to the chemical composition, a very satisfactory level of plasticity and toughness can be achieved by hardening and tempering after appropriate heat treatment for HSLA steel [45]. Surface hardening processes are among the most straightforward and cost-effective ways to enhance iron-based materials' mechanical properties and corrosion resistance [46]. With these methods, quenching, laser hardening, and similar surface modification processes can be performed without any atomic diffusion relying on the chemical combination of the material. On the other hand, nitride, boride, carbide, and aluminide layers can be formed by atomic diffusion toward the material's interior. By forming layers, it can be ensured that the surface is hard, durable, and resistant to

wear, corrosion and oxidation. All these methods absorb energy and provide toughness in materials exposed to static and dynamic loads without causing any hardness changes in the matrix structure. [47,48].

Thermal spray coating, chemical vapor deposition, physical vapor deposition, and laser treatment applications are the leading methods of thermochemical surface hardening and coating methods, such as carburizing, boronizing, nitriding, and aluminizing [49]. These methods have some advantages over each other. Thermochemical methods are more valuable because they require more straightforward equipment and lower installation costs than PVD, CVD and laser methods. Moreover, thermochemical methods are more environmentally friendly, and the obtained coating has better adhesion strength to the substrate. However, they have higher hardness values and are resistant to high temperatures (over 800 °C) [50,51]. Among the thermochemical methods, aluminizing is one step ahead with its application to many alloys such as Fe, Ni, Co, and Cr. Also, there is no need for the substrate material to contain a C or N content above a particular ratio to obtain a coating as in some other thermo-reactive diffusion methods (TRD).

Aluminium and its alloys are commonly used for corrosion protection in many industrial applications such as aircraft, rockets, spacecraft, and marine because of their aluminium-oxide forming capability in natural conditions [52]. Therefore, it is unavoidable to use aluminium as a coating material. Aluminide coating layer can be formed by different methods such as hot dip, spraying, electric arc spraying, diffusion coating, cathodic dissipation, electroless metal coating, ion plating and radiation (pack cementation). However, it should be noted that pack-aluminizing is a pretty cheap diffusion coating among these techniques [53] and can be effectively applied to various sizes and geometries. Many researchers have used the pack-aluminizing process for its advantages [54]. The pack-aluminizing process has been used to overcome corrosion and wear issues of different materials subjected to various working and environmental conditions [44,53,55]. Several researchers investigated the thickness, microstructure, hardness, wear and corrosion damage mechanisms of the aluminizing layer [55–57].

In the present work, pack-aluminizing was applied on R4 grade high strength low alloy (HSLA) offshore mooring chain steel, considering the success of the aluminide coating in enhancing wear, oxidation and corrosion resistance in the literature [44,53,55]. On the other hand, no studies have been found on the effects of aluminizing on offshore mooring chains and/or its effects on corrosion and wear resistance in the open literature. In order to fill this gap in the literature, R4 quality HSLA steel was aluminized for the first time to form a Fe_xAl_y layer with higher hardness and corrosion resistance on the surface at 850 °C for 2 h with 30 % Al, 7.5% NH_4Cl , and 62.5% Al_2O_3 powder mixtures. Then, scanning electron microscope (SEM), energy dispersive spectroscopy (EDS), X-ray diffraction (XRD) analysis, and microhardness tests were employed to characterize of Fe_xAl_y layer. Finally, the wear and corrosion performances of Fe_xAl_y layers were compared with the untreated sample.

2. Materials and Methods

2.1 Sample preparation and coating

Offshore mooring chains and accessories are produced from HSLA steels and classified according to their ultimate strength [32,33]. In the study, the R4 grade alloy was selected as the substrate because of the most used grade in practice and is suitable for the pack aluminizing process. R4 grade alloy is hot rolled round bar steel and contains a minimum of 0.20% molybdenum according to spectrometric analysis. The chemical composition of R4 steel used in this study was presented in Table 1. Before the coating process, steel samples

were cut in dimensions of (23 x 10) mm and 10 mm thickness with a precision cutting device from a real 76 mm diameter R4 grade chain link and the aluminide layer was deposited by the pack cementation method. Sample surfaces were sanded with 320-400-600-800-1000-1200 SiC papers, respectively. Then, the samples were subjected to ultrasonic cleaning with an alcohol bath for 15 minutes.

Table 1 Chemical composition of R4 steel used in the study

Element	Fe	Mo	C	Mn	Cr	Ni	Others
wt. %	95.90	0.20	0.25	1.60	0.6	0.7	0.75

Previous studies [52,54] show that the aluminization process comprises 30% Al, 7.5% NH_4Cl , and 62.5% Al_2O_3 powder mixtures by weight. To form the aluminide layer, the samples were placed in stainless steel crucibles, with each piece surrounded by a layer of aluminizing powder 10 mm thick on all sides. The crucibles were tightly sealed using fasteners and placed into a preheated atmospheric muffle furnace to the aluminizing temperature (850 °C), and the crucibles were kept for 2 hours. Then, the crucible was taken from the furnace and air-cooled to room temperature. After cooling, the dust residues were cleaned from the surface of the samples. A representation of the aluminizing process is shown in Fig. 1.

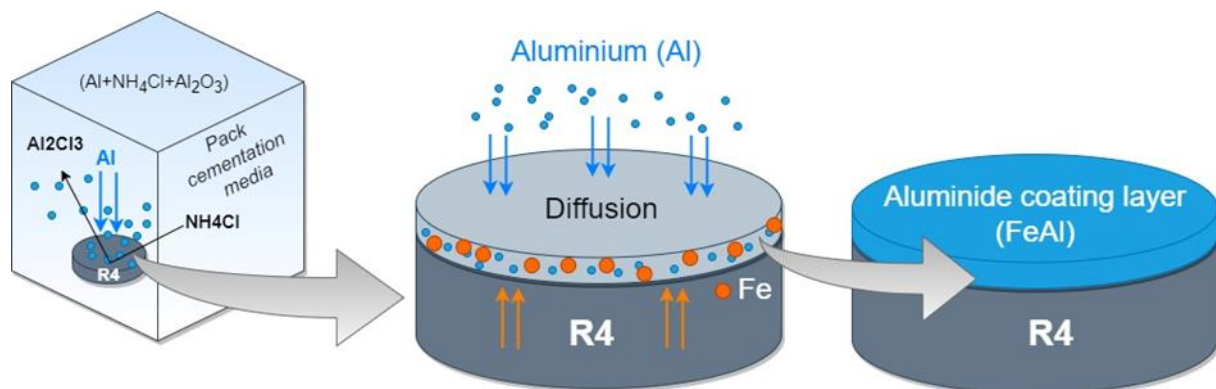


Fig. 1 Schematic representation of the aluminizing process

The coated samples were cut to (10x10x10) mm with a precision saw and were cold-moulded to reveal cross-sections of the iron-aluminide layer. The samples were prepared by embedding them into the bakelite and mechanically ground from the cross-section with 320–2000 size SiC sheets. Afterward, the grounded samples were polished with 3 μm and 1 μm Al_2O_3 solutions to obtain a mirror-like surface and finally subjected to 5 percent Nital solution for 6 s to display fine details of the microstructure.

MAIA3 XMU model SEM (TESCAN) and X-Max model EDS (OXFORD) were used to characterize microstructural properties and distribution of the Fe_xAl_y coatings. SEM and EDS studies were executed with a 10-kV acceleration voltage and 11 mm spot size to more clearly evaluate the diffusion of the elements in the obtained coatings from the surface to the substrate. The investigation of alloying elements (Fe, Al, Cr, Ni and Mn) distribution in the coating layer was done by EDS analysis. The Fiji ImageJ measurement program was used to determine FeAl coating thicknesses based on images taken from SEM on an average of 5

measurements. XRD patterns were analysed with Rigaku smart LabTM with Cu K α radiation $\lambda=0.154$ nm with scan step size 0.0525211 and 2 θ angles ranging from 0 to 90°. Microhardness measurement was performed with a Vickers pyramid-tip Future-Tech FM-700 hardness device by applying a 100-gf load and 15 s dwell time along a line from the surface of the coating layer towards the interior to characterize the hardness change in the coating layer, transition zone, and matrix.

2.2 Corrosion and tribocorrosion test procedure in situ

The tribocorrosion performances of the untreated and aluminized R4 grade steel samples were performed in a linear reciprocating type wear device (TURKYUS) coupled with a potentiostat since mooring chains service in the air and marine environments. Fig. 2 shows the experimental arrangement used in the study. This arrangement permits the simultaneous observation of mechanical and electrochemical parameters during the tests. In corrosion and tribocorrosion tests, 3.5% NaCl electrolyte was prepared and used to simulate seawater, and 150 ml of this electrolyte was filled into a Delrin-made cell in each trial. The corrosion cell and ball holder were made from Delrin (a polymer material) to avoid undesirable corrosion effects during the tests.

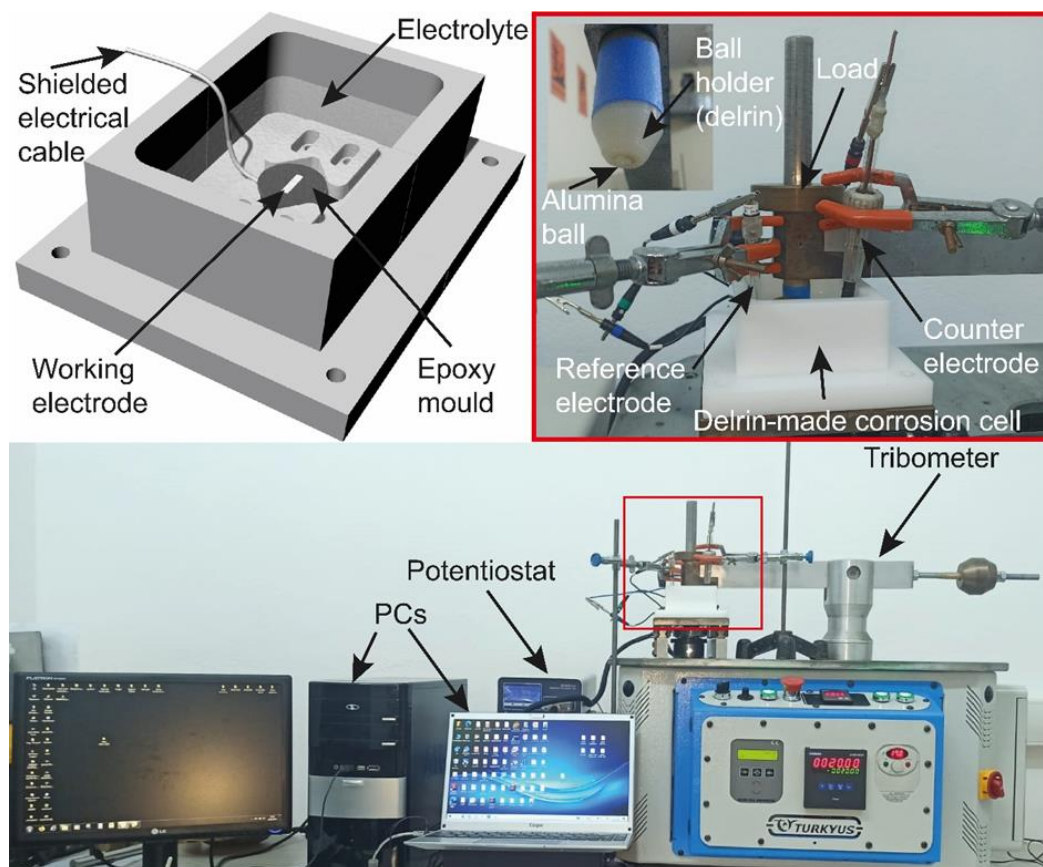


Fig. 2 Tribocorrosion test set up

The abrasive counter body employed a 6.35 mm diameter sintered hard alumina (Al_2O_3) ball with a hardness of 14 GPa. The alumina ball represented a 6 mm wear stroke with a sliding speed of 0.02 m/s, and a 36 m total wear path was achieved in sliding tests. Hertzian Contact Theory was followed to calculate the contact conditions, considering the contact pressure between the chain links in the actual situation, as was done in previous studies

[22,41]. The 5 N load was applied in the study, corresponding to an average Hertzian pressure of 1216.2 MPa with a circular contact area diameter of 0.089 mm.

The dimensions of (23 x 10) mm, and 10 mm thickness samples were prepared and moulded with epoxy to have a contact area of 2.3 cm² with the electrolyte. The samples were smoothed by grounding with 1200 grit SiC paper and cleaned ultrasonically in an acetone bath for 30 minutes after being immersed in 5 M HCl acid for 5 minutes. Before the corrosion and tribocorrosion tests, the samples were dried in an oven up to 200 °C to be ready. Afterward, the samples were placed into a Delrin-made corrosion cell to measure open circuit potentials (OCP) for 1 hour. In corrosion and tribocorrosion tests, Ag/AgCl (+ 197 mV versus standard hydrogen electrode) electrode was used as a reference electrode, platinum as a counter electrode and coated/uncoated R4 steel samples were used as the working electrode. An analyser test device (Zive SP1) and a conventional three-electrode system were used for all electrochemical experiments. A corrosion analysis software (Zive Data Manager) was used to measure corrosion potentials (E_{corr}) and calculate the corrosion current densities (i_{corr}). The OCP test and Tafel extrapolation methods (ASTM G5-14) were used to determine corrosion potential and current density, respectively. The samples were immersed and waited in the electrolyte for 3600 s to stabilize the electrochemical potential before all tests.

Potentiodynamic polarization tests were performed on both corrosion and tribocorrosion conditions under 5 N loads to assess the effect of the sliding wear on corrosion kinetics in simulated seawater. The potential varied from -1 V to 0.4 V concerning each sample's OCP (vs. Ag/AgCl) at a scan rate of 0.166 mV/s. The sliding tribocorrosion test was continued for 30 min, and the coefficient of friction (COF) was recorded during this time under cathodic, open circuit and anodic potentials. The cathodic potentiostatic tribocorrosion tests were conducted on both coated and uncoated R4 samples at the constant applied potential of -0.85 V to measure the pure mechanical wear and evaluate the synergistic effects between wear and corrosion. According to the polarization data, -0.85 V potential was selected because of remaining in the cathodic region for both R4 alloy and aluminide coating. There is no electrochemical corrosion under such potential and material loss from the wear track is ultimately due to pure mechanical wear in the electrolyte. In the study, -0.15 V anodic potential was also selected and applied to understand the anodic dissolution of the aluminide layer according to polarization curves.

All tests were replicated at least three times to increase the accuracy of the data obtained from the test results under the same conditions, and the average value was taken. The experiments were employed at 23±2 °C room temperature.

2.3 Determination of material loss and surface morphology

A 3D laser scanning microscope (Filmetrics Profilm 3D) was used to measure the size of the wear tracks formed after the tribocorrosion tests to define the wear mechanism. The total volume loss of each track was calculated by integrating the cross-sectional areas of wear profiles obtained in 5 different locations using the microscope along the wear track length. In addition, the surface morphology of the tested samples under different electrochemical conditions was analysed after each corrosion and tribocorrosion test using an SEM instrument provided with EDS capabilities.

3. Results and Discussions

3.1 Characterization

Fig. 3 shows the aluminide layer's morphology, SEM section and EDS line analysis. EDS line analysis in Fig. 3, the presence of three regions after the aluminization process

draws attention. These regions are (i) a coating layer with approximately 60% Al and 40% Fe atomically throughout the coating layer (in the range of 0-100 μm), (ii) a transition zone where the presence of aluminium decreases in the range of 100-120 μm and (iii) beyond 120 μm is the substrate. The existence of the transition zone is essential in thermochemical coatings. Because of the transition zone contributes to the bonding of the coatings to the substrate material with a further adhesion force and thus provides higher abrasion resistance [51,58–60]. Sun et al. [61] explained the transition zone formation in the aluminide layer as forming an iron-aluminium alloy layer, where the active aluminium atoms first adhere to the substrate surface and dissolve in the steel to form a solid solution. The aluminium atoms rise to a specific concentration depending on temperature and time [61]. After this formation, the aluminized layer gradually thickens due to the displacement (diffuse) of aluminium and iron atoms replacing each other. The aluminium ratio in the environment is critical in forming the alumina layer. In the study, while it was formed at a constant rate (60% Al) throughout the coating layer, the formation of an aluminide layer with different Al contents was observed on the surface towards the inner parts by Sun et al. [61].

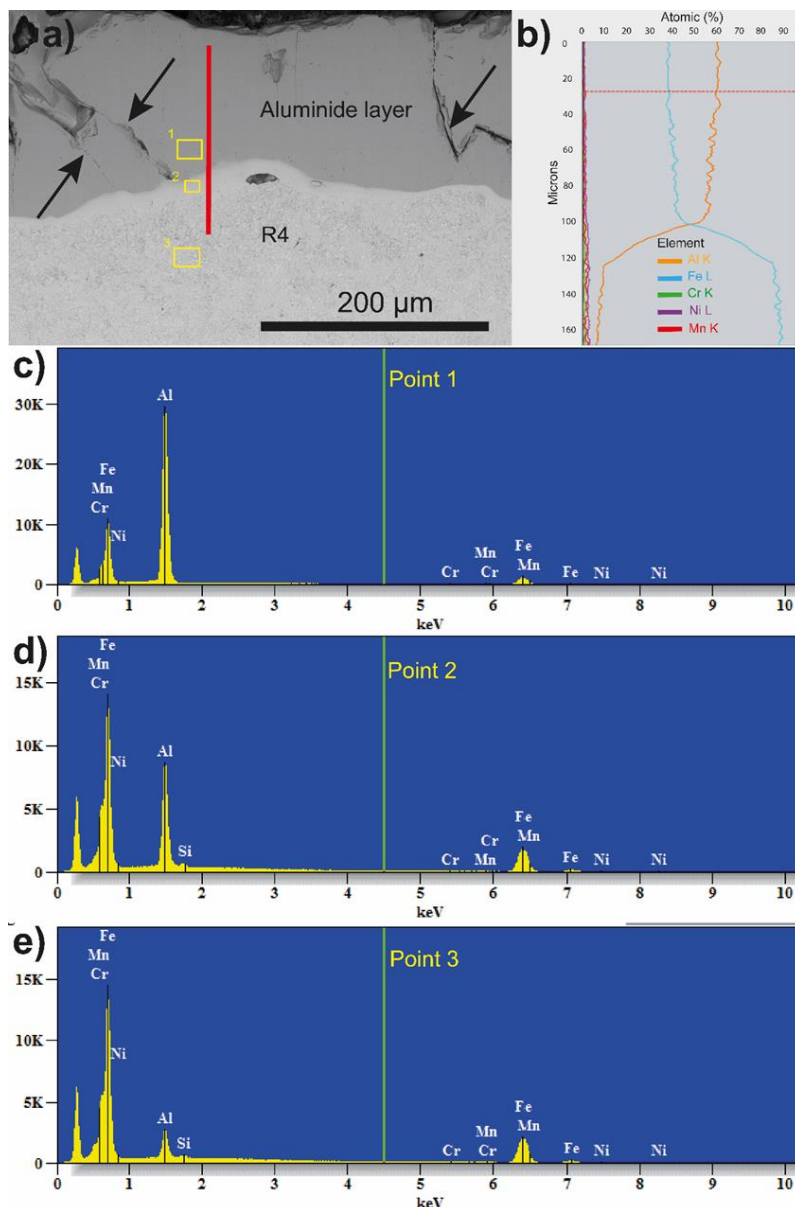


Fig. 3 SEM sectional view and regional/spot EDS analysis of aluminized R4 sample

Some cracks in the aluminide layer were determined and illustrated with black arrows in Fig. 3(a). Cracks, discontinuities, surface roughness, and porosity are essential to mechanical properties [62] and corrosion resistance. They often act as starting points for corrosion, wear, and fatigue failures and can reduce the material's service life [63,64]. Al and Fe distributed nearly 60% and 40% ratios in the coating layer, respectively. In Fig. 3(b), it is evident from the EDS analysis that the coatings are composed of Al-rich phases after being aluminized. These values detected in the EDS results confirm the dominant FeAl and minor Fe₂Al₅ phases in XRD analysis. Spot EDS analyses were taken from the coating, transition and base material and showed Fig. 3(c,d, and e). Fig. 3(c) shows the coating layer's high ratio of Al. Al, Cr, Mn and Fe were evident in the transition region, with Al in Fig. 3(d) and Fe content in Fig. 3(e).

Fig. 4 shows the XRD diagram of R4 steel and aluminide coating. The most intense peak of the untreated R4 material is the reflection from the (110) plane, and its angular position is $2\theta = 44.99^\circ$. Also, it was determined that the 200 and 211 planes of the minor phases belong to α -Fe. The Cr peak was detected in the structure at $2\theta = 54.65^\circ$. On the other hand, the most intense peak is FeAl in the aluminized sample and belongs to the (110) plane, and its angular position is $2\theta = 42.65^\circ$. Fig. 4 confirms the presence of different aluminide formations on the coating layer. Similarly, Öksüzoğlu and Döleker reported that FeAl₂, Fe₂Al₅, FeAl and Al₅FeNi phases were formed in their aluminization studies on 904L stainless steel [65].

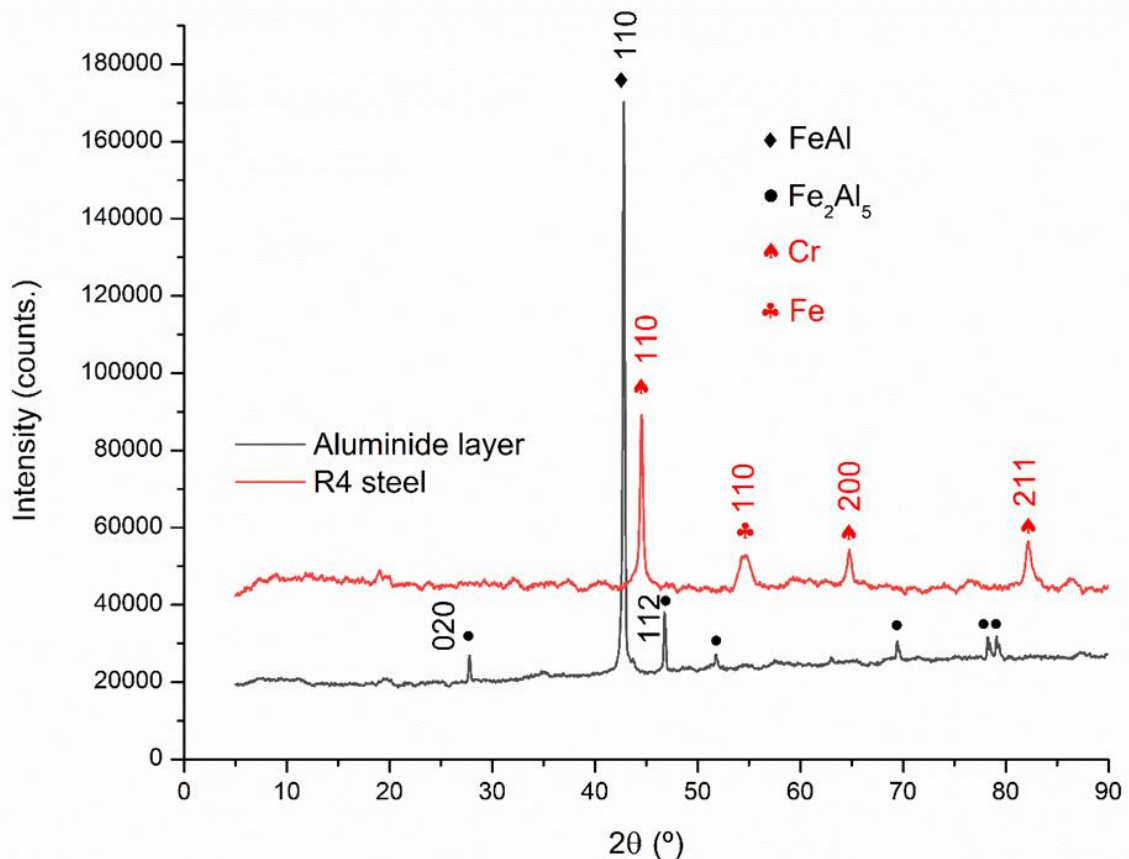


Fig. 4 XRD results of R4 and aluminide coating

Moreover, minor Fe₂Al₅ phases were also placed in the coating structure. The forming of FeAl and Fe₂Al₅ phases on the surface of the samples is significant. Because as seen in the

Fe-Al phase diagram in Fig. 5, FeAl maintains its stability up to 1310 °C, while Fe₂Al₅ is up to 1169 °C, whereas the melting temperature of Al is 668 °C and the phase change temperature of pure iron is 723 °C. Therefore, FeAl coatings formed on the surface can continue to exist on the surface up to high temperatures.

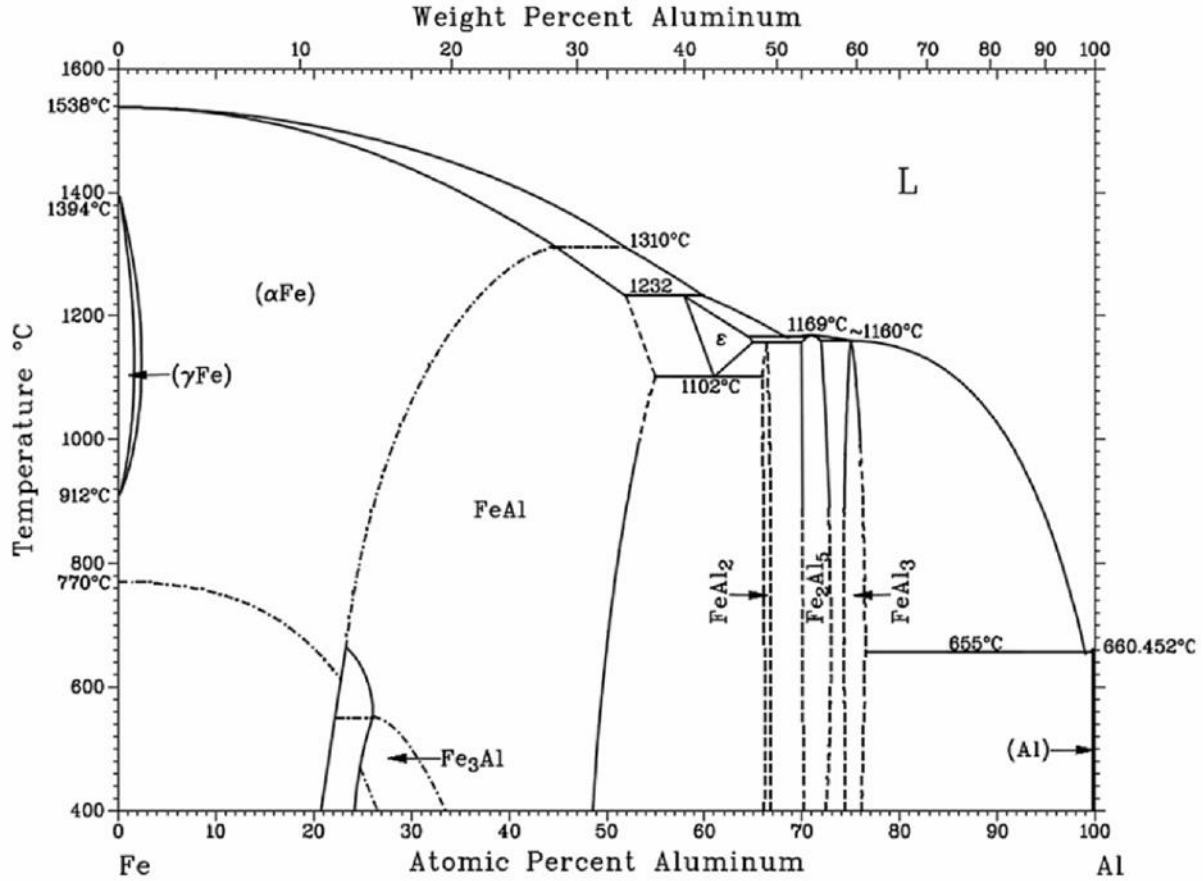


Fig. 5 Fe-Al equilibrium phase diagram [66]

Hardness is an essential criterion in determining wear resistance. Fig. 6 shows that the hardness values obtained from the aluminide coating are 555.5-831.5 HV0.05 and higher than R4 steel due to the cementation [67]. The lowest hardness value in the coating layer was obtained close to the surface as 555.5 HV0.05 due to the crack formed during the measurement. Fractures of the samples near the surface may be due to the NH₄Cl. As it is very well known that the use of F(fluorine)-compounds lead to M-F (M: metal) evaporating from the surface during the surface treatment, it can be caused the formation of the void between the substrate/coating and surface of layers [68]. In the transition region of the substrate side, the hardness nearly decreased by half, according to Fig. 6. The higher hardness values in the coating layer can be associated with forming the FeAl phases, and similar results were observed for the pack aluminizing process of steels in different studies [56,67].

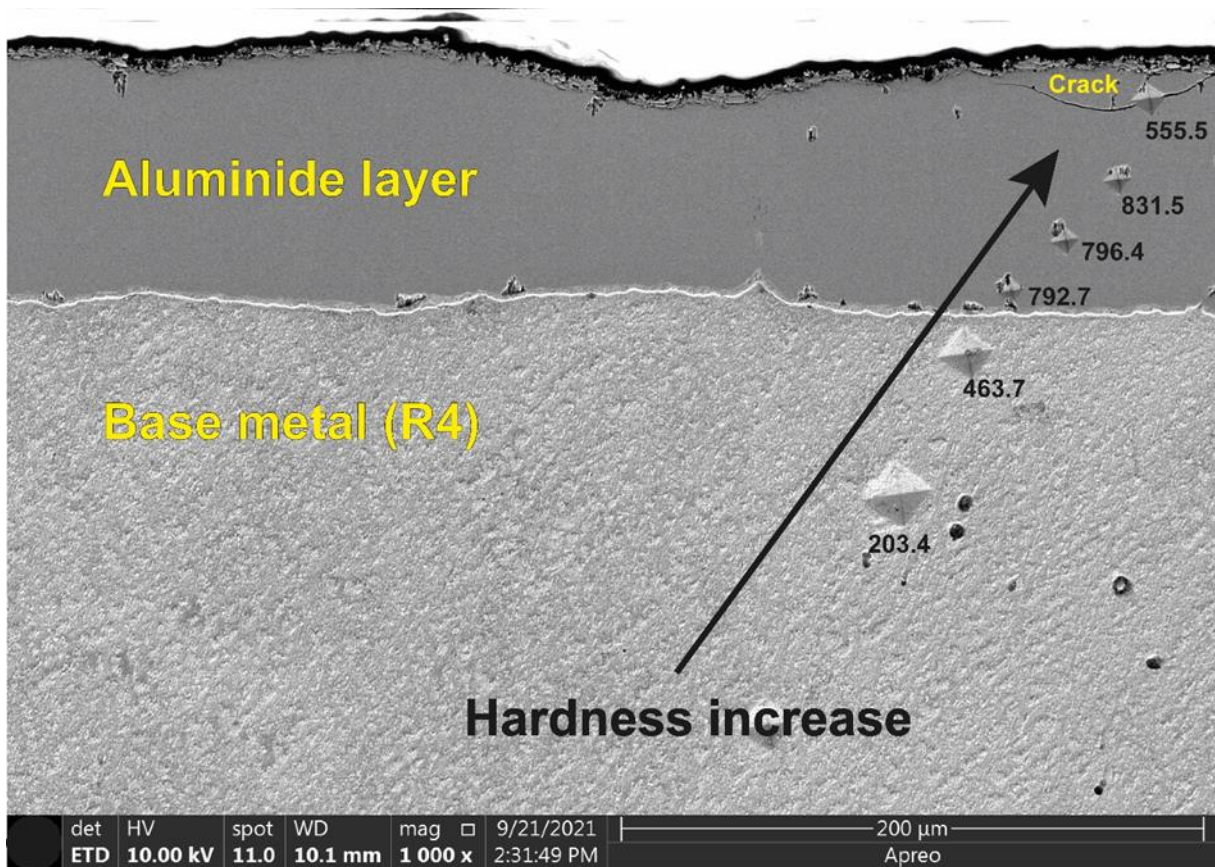


Fig. 6 Hardness distribution in the aluminide layer and base material.

3.2 Corrosion and tribocorrosion test results

3.2.1 Potentiodynamic polarization under corrosion and tribocorrosion conditions

Fig. 7 depicted potentiodynamic polarization scans employed to understand corrosion kinetics from 0.4 V to -1 V under corrosion and tribocorrosion conditions. Table 2 presents the electrochemical data obtained from standard Tafel polarization curves for R4 and aluminized R4 under corrosion and tribocorrosion conditions in 3.5% NaCl. Although the corrosion potential values acquired for the aluminide coating are close to the R4 steel substrate, the corrosion current density is higher and better than nearly 6 times in corrosion and 2 times fold in tribocorrosion conditions, according to Table 2 and Fig. 7.

A comparison effect of the surface treatment of R4 on corrosion is presented in Fig. 7(a) and for tribocorrosion conditions in Fig. 7(b). The aluminium coating improved the corrosion resistance of the untreated R4 sample according to the polarization scans only in the corrosion state. The aluminide layer provides lower corrosion currents, significantly higher corrosion resistance and lower corrosion rates than untreated R4, according to Table 2. When the aluminium layer contacts the electrolyte, it forms an oxide layer over the entire area, and this behaviour resembles passive materials such as stainless steel. The ceramic structure of the aluminium coating and the higher chemical stability of the aluminide oxide layer in NaCl electrolyte provides better corrosion resistance by serving as a barrier against the underlying steel substrate [41].

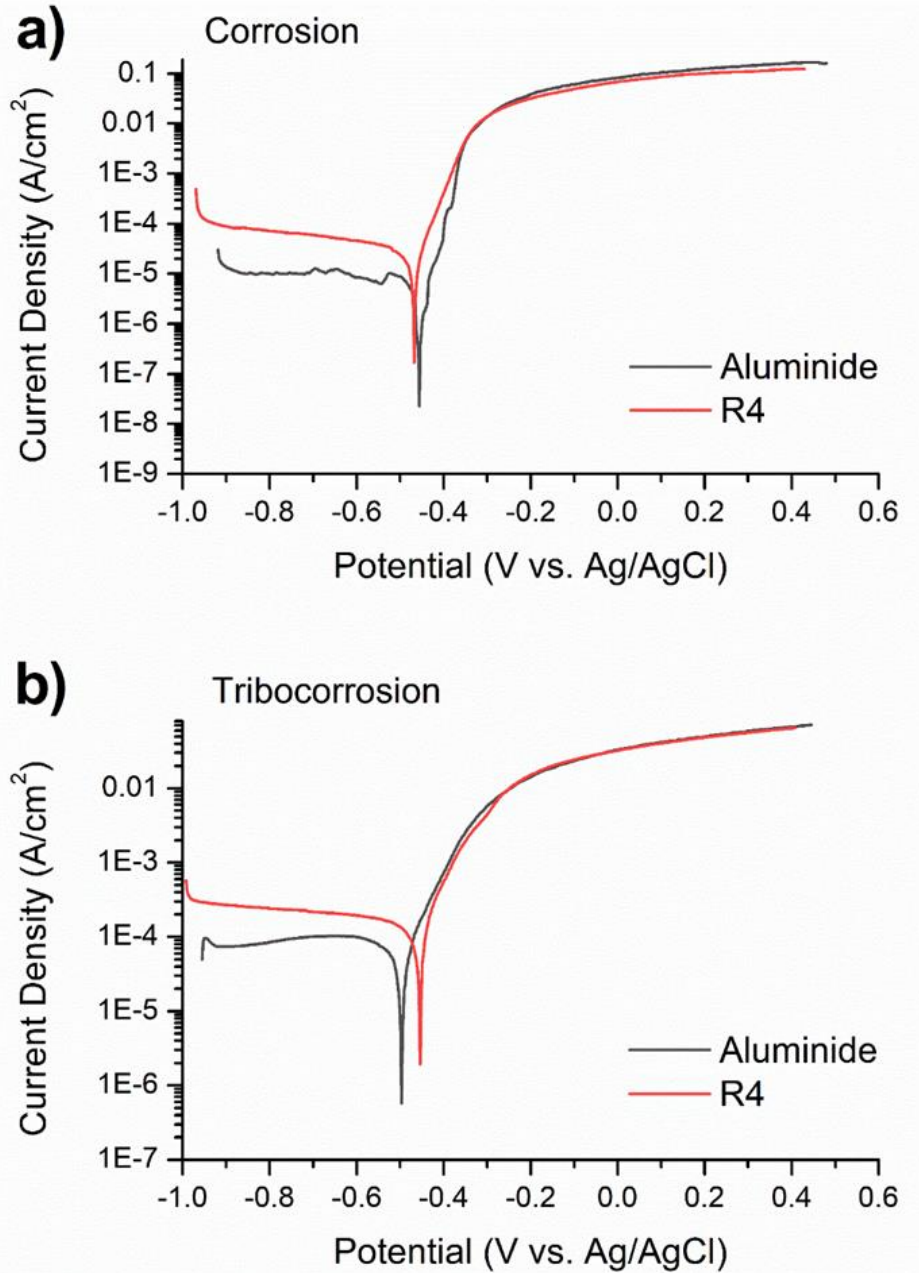


Fig. 7 Comparative evaluation of potentiodynamic scans under a) corrosion (without sliding) and b) tribocorrosion (5 N load) conditions

Table 2 Electrochemical data obtained from the polarisation curves under corrosion and tribocorrosion conditions for R4 and aluminized R4 steel in 3.5% NaCl by Tafel extrapolation

	Corrosion		Tribocorrosion	
	R4	Aluminized R4	R4	Aluminized R4
E_{corr} (mV)	-466	-444	-454	-494
I_{corr} (A/cm ²)	2.03E-5	3.59E-6	1.13E-4	5.09E-5
Corr Rate (mmpy)	0.4653	0.0823	2.5788	1.1666

Tribocorrosion conditions presented in Fig.7(b), the untreated R4 and aluminized samples exhibited the opposite behaviour concerning each other. The electrochemical behaviour of both R4 steel and aluminized samples changed under sliding conditions because mechanical effects caused the deterioration of the surface structure. While the corrosion potential of the aluminium coating under mechanical contact decreased, the corrosion potential of the untreated sample increased. The reason for this situation is that the formation of an oxide layer on the surface of the aluminium coating provides a passive protective layer, while the untreated R4 steel is exposed to more dissolution from the area outside the wear track since it is an active material. The difference in current values measured under corrosion and sliding tribocorrosion conditions shows that the corrosion kinetic in the wear track and the unworn surface is different due to the continuous mechanical action of the counter body. This phenomenon inhibits the corrosion tendency of the material within the wear track. In Fig. 7, Although there is no clear passive region for both R4 and aluminized R4, the aluminized samples performed passive-like behaviour according to corrosion potential changes when comparing corrosion and tribocorrosion conditions. In Fig. 7(b), the degradation of the passive film layer resulted in a sharp increase in current density by several orders of magnitude with minor potential variations due to trans passive dissolution and oxidation processes. Aggressive ions such as Cl^- in seawater cause the passive layer to deteriorate [39,41,69,70]. These ions, which have small sizes, pass through the passive film and cause the dissolution of aluminium oxide. The continuous deterioration of passive film causes local corrosion [69,71,72] and leads to steel release with the rapid dissolution of aluminium, especially at higher anodic potentials. Anodic polarization increases substrate corrosion due to the decrease in aluminium layer thickness.

3.2.2 Evaluation of OCP with and without sliding

Fig. 8(a) shows the open circuit potentials of the samples which are kept in 3.5% NaCl solution for 3600 s immersion. The electrochemical potential of R4 steel decreases during the immersion period and reaches a value of around -0.57 V at the end of 3600 s. The drop-in potential is attributed to corrosion processes on the surface, mainly forming a rust layer in this type of carbon steel primarily consisting of iron oxyhydroxide (FeOOH) compounds [39,41,70,73]. The porous and low-adherent nature of this rust layer makes it unable to form an effective barrier for the electrolyte. However, after a certain period, the rust layer can thicken and prevent oxygen from reaching the abrasive surface [71], and the system stabilizes.

The aluminide coating showed a more stable potential response in the first hour of immersion than R4 steel. The formation of an oxide layer of a few nanometres thickness, which provides a barrier effect on the surface, caused a slight increase in potential compared to R4 steel. The more stable potential obtained after the first hour of immersion for aluminide coating was around -0.52 V in a simulated marine environment. Although there are slight variations in the OCP of aluminized R4 during the immersion period in Fig. 8(a), there is no significant substrate contribution to the potential due to the excellent protection effect of the aluminide layer. After 2700 s of immersion period, the partial reduction in open circuit potential can be ascribed to the porous nature of the aluminide coating [57]. The porosity and looseness of the outer layer may have caused the electrolyte to penetrate rapidly through the pores, causing a decrease in potential. The higher potential of the aluminide layer compared with the untreated samples showed that the aluminide layer provides adequate seawater protection.

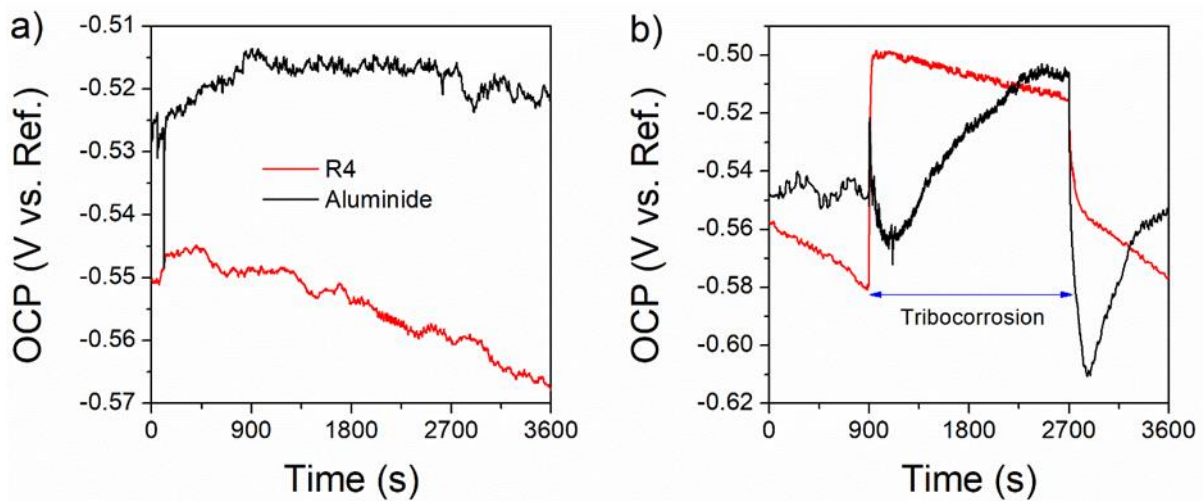


Fig. 8 OCP changes during a) 1 h immersion and b) under sliding conditions

Fig. 8(b) shows the evolution of OCP during the sliding. Sliding contact caused a shift in electrochemical potential towards more positive values for R4 steel due to the inhomogeneities between the worn and unworn surfaces of the material. The two regions behaved as batteries because of the potential difference. The destruction in the wear track region increased the potential difference between worn and unworn zones in the sample and caused a shift in OCP. The continuous mechanical action of the alumina counter body resulted in the subtraction of material from the top surface and this directed the kinetics of corrosion in the track. This result caused a slowing corrosion process in that area for HSLA R4 steel. The wear track exhibits cathodic behaviour and the potential difference between the two regions causes corrosion-induced material loss from the unworn region behaving more anodic than the wear track. Although a rust layer cannot form on the wear track due to continuous mechanical effects, it is evident that a rust layer is included in the non-abraded region, reducing the corrosion rate over time. After the sliding period, the surface on the wear track reacted with the electrolyte again and formed a new rust layer, which allowed the material to reach a value close to its potential values before sliding. In addition, some researchers claim that the pits and the rust layer on the surface in carbon steels immersed in NaCl solutions prevent oxygen diffusion on the surface [39,41,70,73] and restrict the rate of deterioration over time.

In the case of aluminide coating, the potential dropped to more negative values during the first 300 s sliding periods in Fig. 8(b). This behaviour can be explained as removing the protective layer from the wear track due to sliding and, thus, the initiation of corrosion dissolution processes. After 300 s of sliding, the potential of the aluminide layer increased due to exposing and leaking the electrolyte to the steel substrate. The potential continuously increased up to R4 potential under sliding conditions and stabilized around -0.51 V. When friction ends, the potential decreased again and the passivation of the worn surface was provided after 900s. The shift in potential indicates that the corrosion kinetics cause a potential difference between the two regions due to the continuous action of the alumina ball on the wear track. The removal of material and corrosion products from the wear track affects the corrosion kinetics in that area. The aluminide layer performed passive-like behaviour in the initiation of sliding, but a time later, cracks and pits/voids in the coating layer might cause leaks towards the substrate, which increased potential. The potential of the aluminide layer

decreased at the end of the sliding period around 2700 s and then repassivation was provided by the aluminide surface. Fig. 8(b) shows that while the potentials of aluminium coating and R4 steel are at the same value, around 2150 s, the coating layer tends to repassivate more than R4. This situation can be explained by the passive layer-forming ability of the aluminium coating.

3.2.3 Potentiostatic tribocorrosion tests and COF assessment

Potentiostatic tribocorrosion tests were conducted to examine the wear and corrosion behaviours of R4 alloy and the aluminized R4 at constant potential under sliding conditions. The applied potentials, both cathodic and anodic, were determined by considering polarization curves. A cathodic potential of -0.85 V was decided and applied to both R4 and aluminized R4 samples to assess pure mechanical wear contribution to total material loss according to the ASTM G119 standard. In the experiment series, an anodic potential of -0.15 V was also applied to aluminized R4 sample to understand further the anodic dissolution behaviour of the coating layer under tribocorrosion conditions.

The currents registered at -0.85 V cathodic potential during sliding on the R4 steel and aluminide layer are negative and have decreasing trends, according to Fig. 9(a). The negative current values show that the cathodic protection has been provided under potentiostatic sliding conditions for the samples. In Fig. 9(b), the current of aluminized R4 increased sharply up to 0.03 A in the first 200 s and then continued from 0.035 A to nearly 0.04 A under applied anodic (-0.15 V) potential. A positive value of the measured current proves the anodic dissolution of the coating layer. Fig. 9 shows that the cathodic protection provides lower current values and is more successful in the aluminium coating.

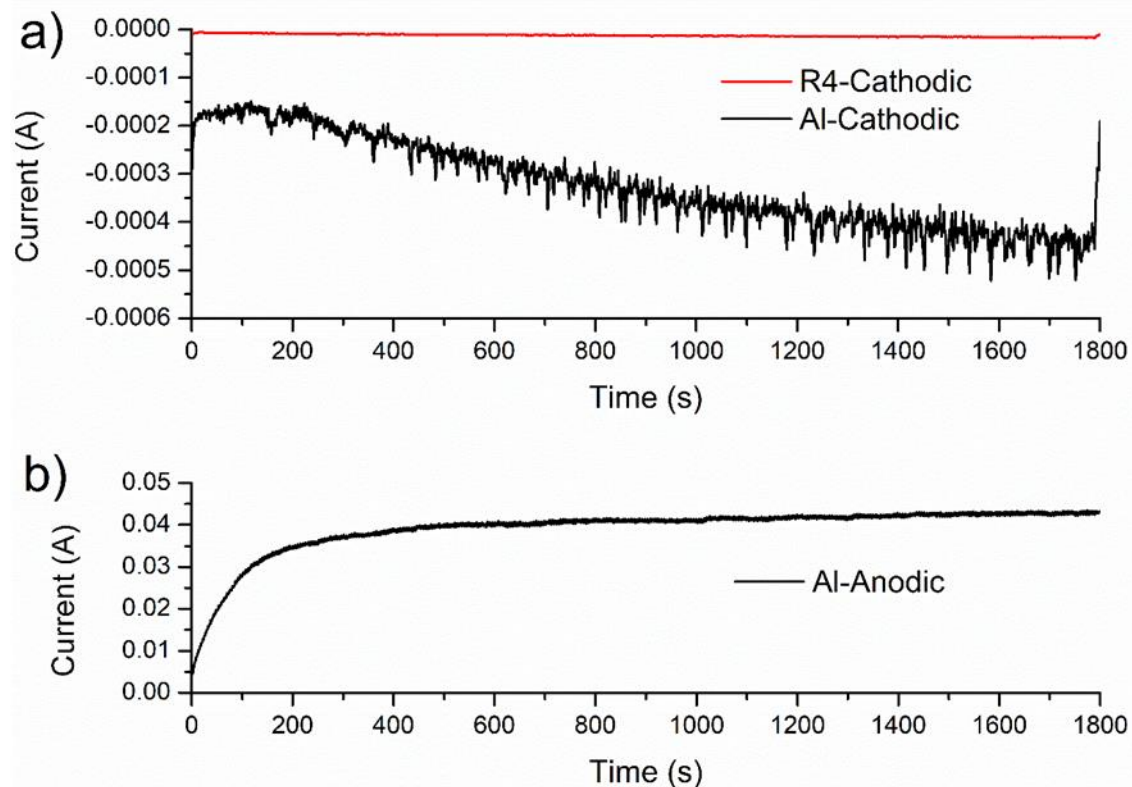


Fig. 9 The current change in potentiostatic tribocorrosion tests under 5 N load a) -0.85 V cathodic potential for R4 and aluminized R4, b) -0.15 V anodic potential for aluminized R4

The registered COF values under sliding potentiostatic tests are depicted in Fig. 10. The COF values showed nearly similar behaviour with time for R4 and aluminized R4 and the results were also compatible with previous studies [41,70]. At the -0.85 V cathodic potential of R4, the continuous action of the counter body tore off the material (Fig. 13) in the contact area because of pure mechanical movement. The formation of third bodies in the wear track can cause a gradual increase in the COF with more significant debris in the tribological contact. However, the reduction in COF observed beyond 1600 s under tribocorrosion test conditions may be due to the slight seawater lubricating effect [74,75] and the removal of contact waste attracted by electrolyte movement. The COF at OCP for R4 steel increases slowly with advancing sliding time and finally stays more stable. The increase in the COF can be ascribed to the continued surface change directed by the sliding.

In the case of the aluminide coating, the COF values under different electrochemical potentials were considerably lower than untreated R4 steel in the tribocorrosion tests, according to Fig. 10. The average COF values are low and almost constant for aluminized R4. At the -0.85 V cathodic potential of aluminized R4, pure mechanical effects resulted in a higher COF value than anodic and OCP conditions because of the cathodic protection. The aluminium might detach from the worn surface in the cathodic potential and behave as a third body, especially during the first 400 s sliding. The possible separated aluminium particles within the track increase the tribological contact with each cycle and cause higher COFs. A further surface investigation has been conducted to explain the result. In Fig. 13, the cracks were determined in the wear track of cathodic and OCP samples, which can quickly form third bodies during sliding. COF value at the aluminide layer's natural tribological and corrosion conditions at OCP was lower than cathodic and higher than anodic conditions. The low COF values in the anodic region for aluminized R4 can be attributed to large pits, resulting in reduced contact between the abrasive ball and the surface [72].

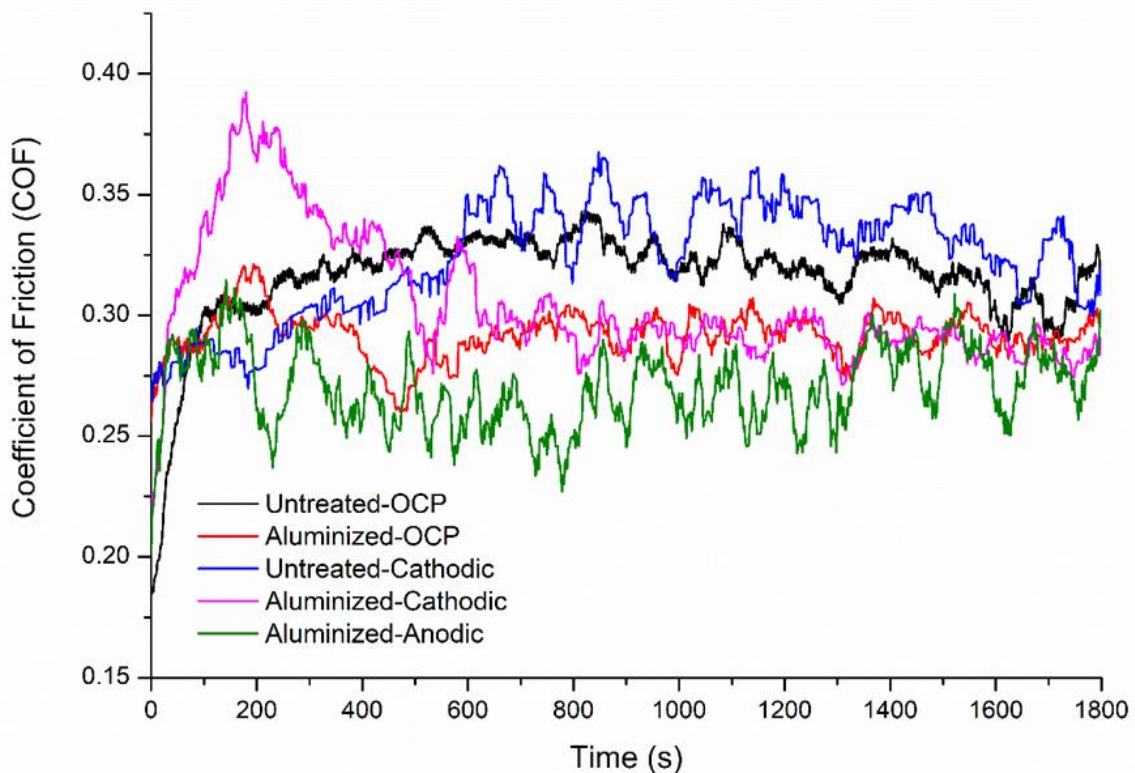


Fig. 10 COF changes over time under different electrochemical sliding conditions

The low coefficient of friction obtained in the aluminium coating than R4 steel can be attributed to two primary factors: Firstly, due to the high hardness (850 HV) created on the surface results in more difficult plastic deformation due to the higher resistance to the pressure exerted by the alumina layer ball. Secondly, the lubricating effect of the aluminium oxide layer formed by the coating on the surface and the rolling motion of the ball rather than cutting. Similar findings were observed on AISI 304 stainless steel with thermochemical boriding [76]. Some studies have also noted that tribocorrosion results in the smoothing of the surface and low viscosity of a thin water film between two hard alumina materials provide hydrodynamic lubrication [77]. The wear residue can be smeared on the tribological contact after a few cycles, thereby reducing the coefficient by providing some lubricating effect. This situation leads to more stable COF values.

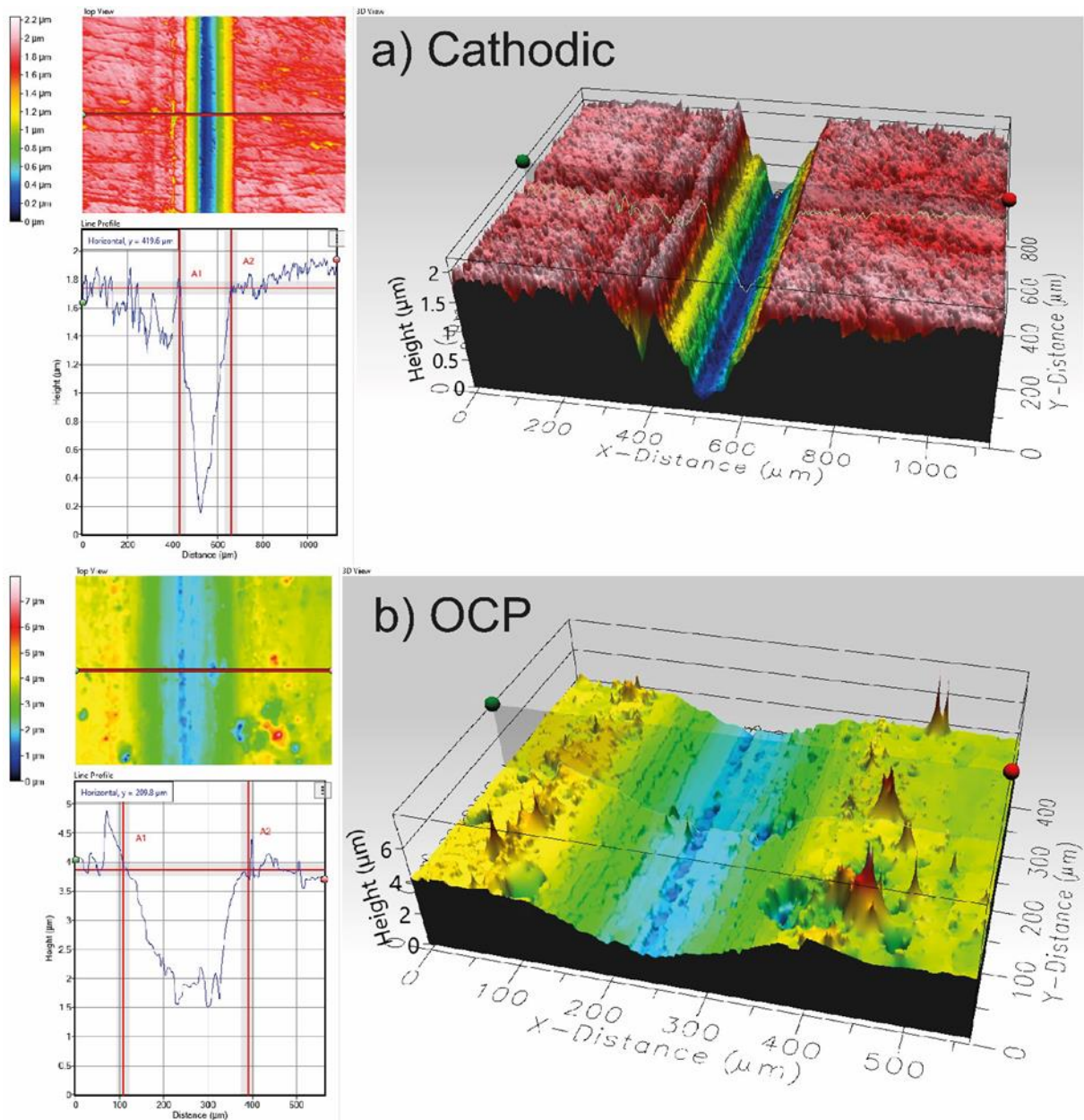


Fig. 11 Optical microscope images of R4 steel tribocorrosion tests under a) cathodic and b) OCP

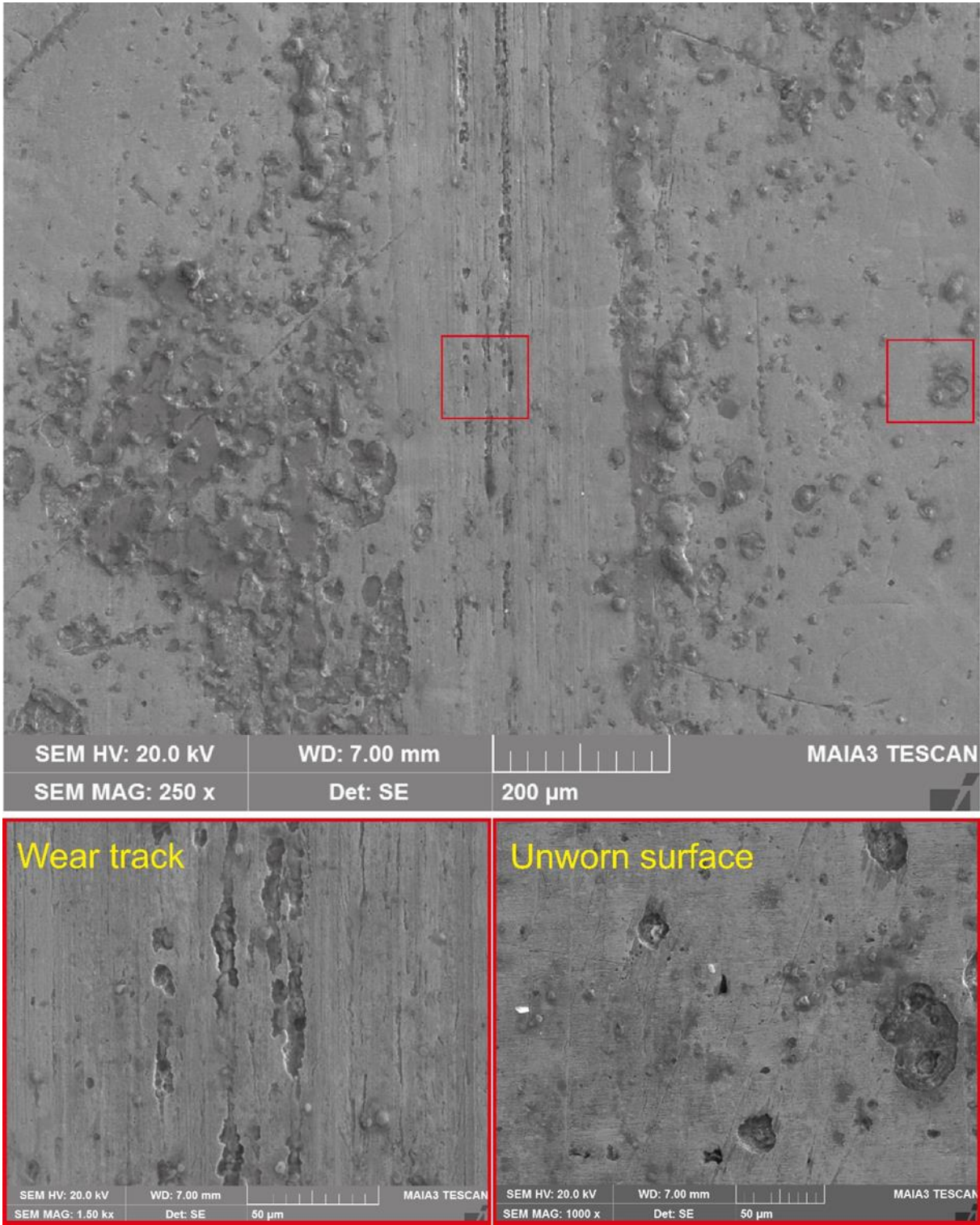


Fig. 12 SEM images after tribocorrosion test of R4 steel under OCP

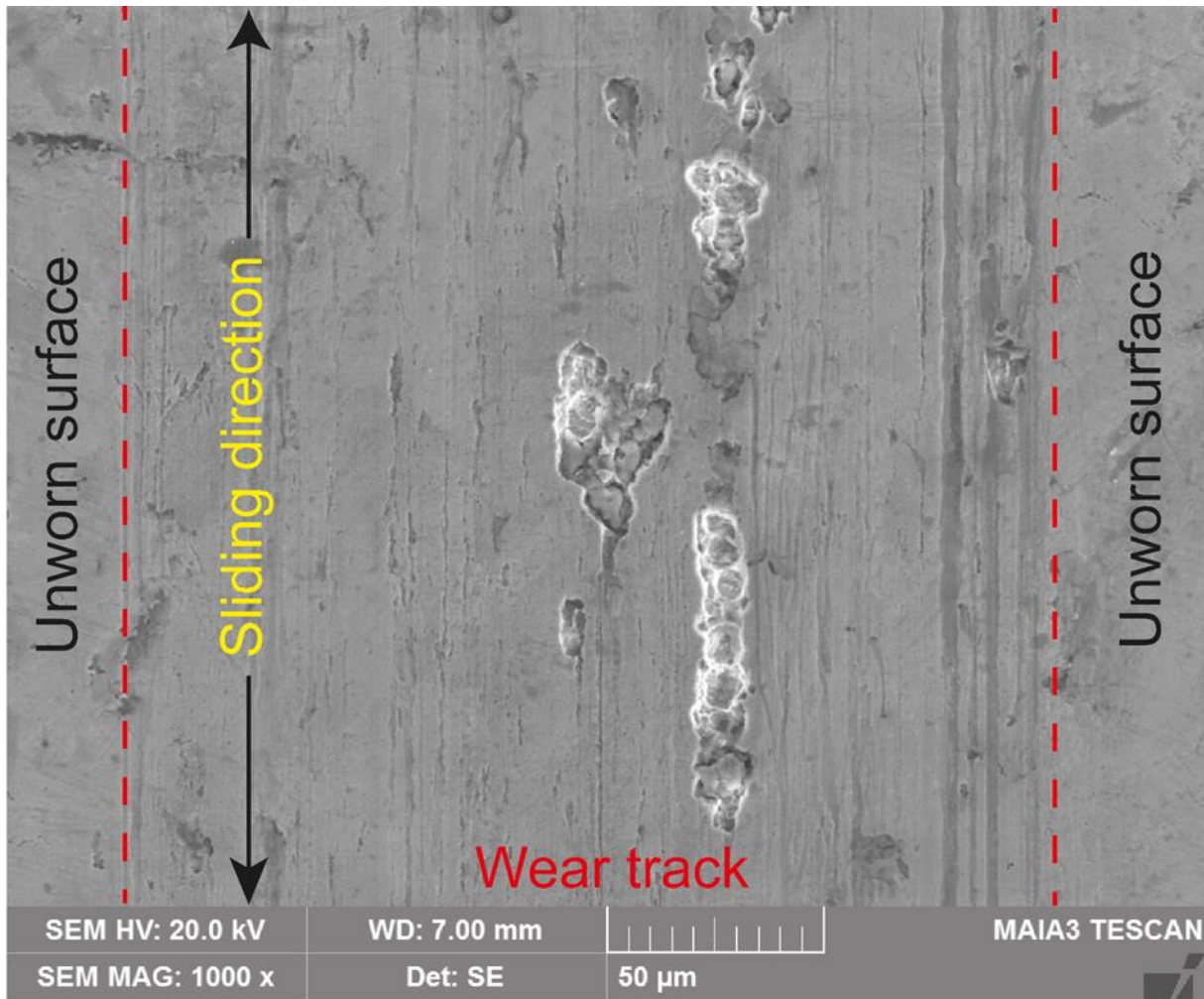


Fig. 13 SEM images after tribocorrosion test of R4 steel under (-0.85 V) cathodic potential

3.3 Surface morphology analysis

After tribocorrosion tests, the surface morphology of the specimens was observed by optical and SEM microscopes. Fig. 11 shows the optical images of the wear track generated on the untreated R4 after the tribocorrosion test under cathodic and OCP. When Fig. 11 was analysed, abrasive effects were evident in the wear tracks. Also, micro-grooving wear marks are clearly visible in Fig. 11. Micro-grooving wear mechanism occurs due to abrasion wastes (hard oxides) separated from the surface during wear, sinking into the surface with low surface hardness and dragging with the ball. Many studies have reported this wear mechanism on surfaces with low surface hardness [78–80].

Furthermore, the wear track width generated under cathodic potential is narrower than OCP. This result could be attributed to the cathodic protection, which provides only mechanical wear without corrosion and decreases material loss. SEM image of the wear track presented in Fig. 11(b) is shown in Fig. 12 and supports the idea that abrasive effects and material detaching were evident with corrosion processes under OCP. The surface of the wear track was observed to be rough and abraded with parallel scratches to the sliding direction. Material smearing in the track was also evident in Fig. 12; corrosion products were visible, especially on the edge of the wear track and unworn surface, indicating more anodic dissolution in that zone. Fig. 12 also provides essential information regarding corrosion

behaviour in the wear track and unworn regions. The dense pitting presence in the unworn area indicates that the anodic dissolution from this region is intense. Fig. 13 depicts the SEM image of the cathodic sample. In Fig. 13, it is clear that the material extraction from the wear track together with parallel scratches to the sliding direction, is evident due to the purely mechanical action of the counter body without corrosion under the cathodic potential. Also, there are no corrosion products in and out of the wear track.

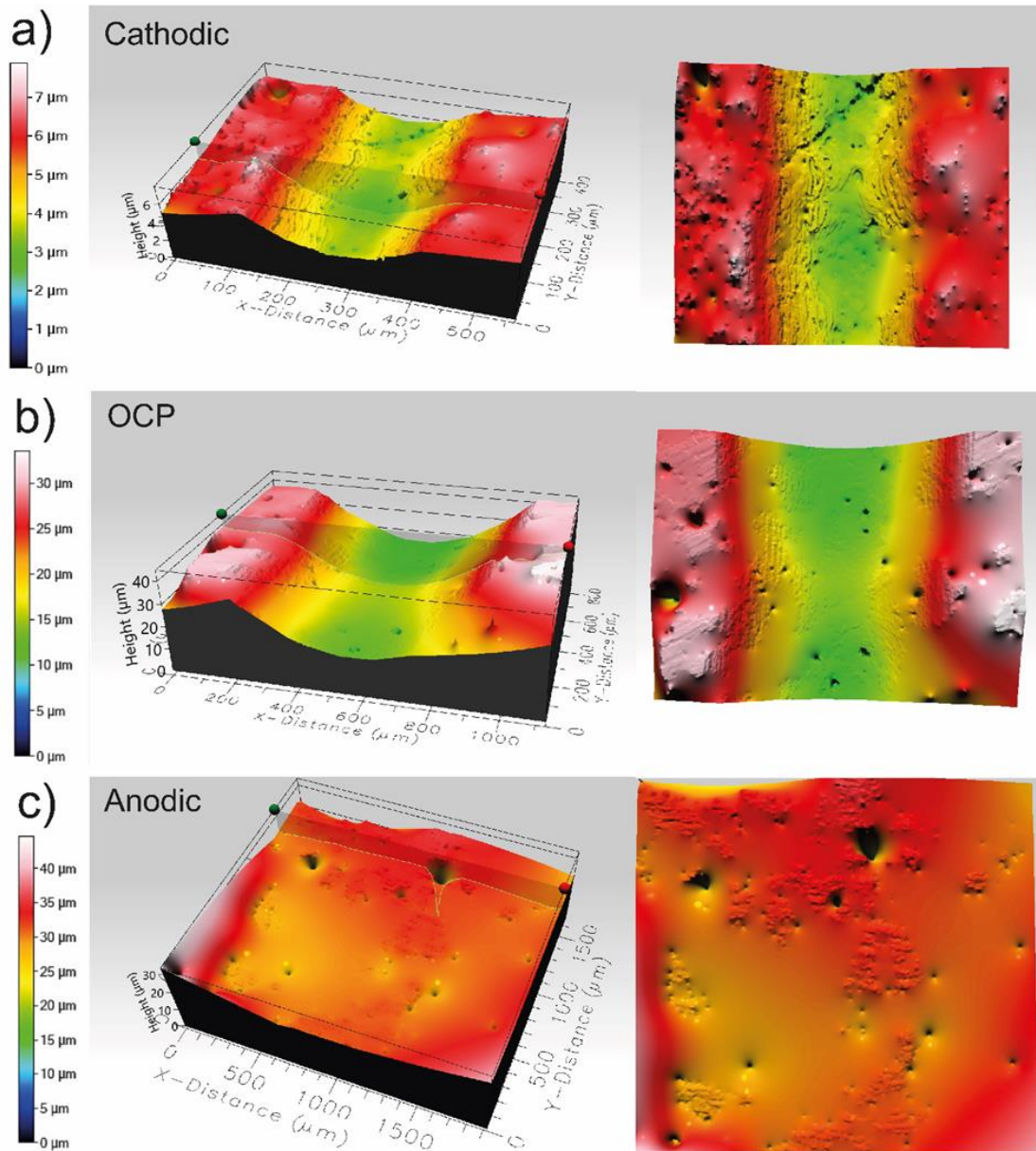


Fig. 14 Optical microscope images aluminized R4 steel under a) cathodic, b) open circuit, and c) anodic potentials

Fig. 14 presents the optical images of the wear track generated on the aluminized R4 by sliding tests for cathodic (Fig. 14a), open circuit (Fig. 14b), and anodic potentials (Fig. 14c). The wear track of the tested sample at -0.85 V cathodic potential is a narrow and irregular surface topography, as seen in Fig. 14(a). Although there was no corrosion in any of the

samples tested at cathodic potential, abrasion lines are evident in the wear track. The small wear volume indicates successful cathodic protection against tribocorrosion at the cathodic potential. The surface morphology of aluminized R4 under OCP showed in Fig. 14(b). The surface state is smooth to that observed at -0.85 V cathodic potential. Pits are also observed inside and outside the track, indicating corrosion. However, the track is broader at an anodic potential of -0.15 V, and the holes are more visible and more profound than the samples tested at -0.85 V cathodic and OCP, according to Fig. 14. In the sample tested at the anodic potential in Fig. 14(c), many large pits spread both the wear track and unworn areas. The steel surface is highly degraded at anodic potential compared to the previous samples shown in Fig. 14(a) and (b). The cross-section profiles of the tracks in Fig. 19 verify that the increase in potential resulted in the track size enlargement for aluminized R4.

Fig. 15 shows SEM images taken from wear tracks of aluminized R4 steel after the tribocorrosion test conducted under cathodic potential in Fig. 15(a) and OCP in Fig. 15(b). Both samples have cracks in their tracks, but the corrosion process is more effective only in OCP. EDS analysis was conducted to understand this phenomenon further, and Fig. 16 was prepared for this aim. In Fig. 16, oxides were evident in the cracks with Cl and Na ions, which supports the idea. It is thought that fractures in the aluminide layer are due to the formation of the brittle Fe_2Al_5 phase, which was formed as a minor, besides the dominant ductile FeAl phase, as determined in the XRD analysis [81]. Because the brittle Fe_2Al_5 intermetallic compound formed on the surface cracks without providing sufficient resistance against any force and falls off on the surface, which damages the mechanical properties [82], this caused the aluminide layers to provide lower wear resistance than the unaluminized samples under tribocorrosion conditions.

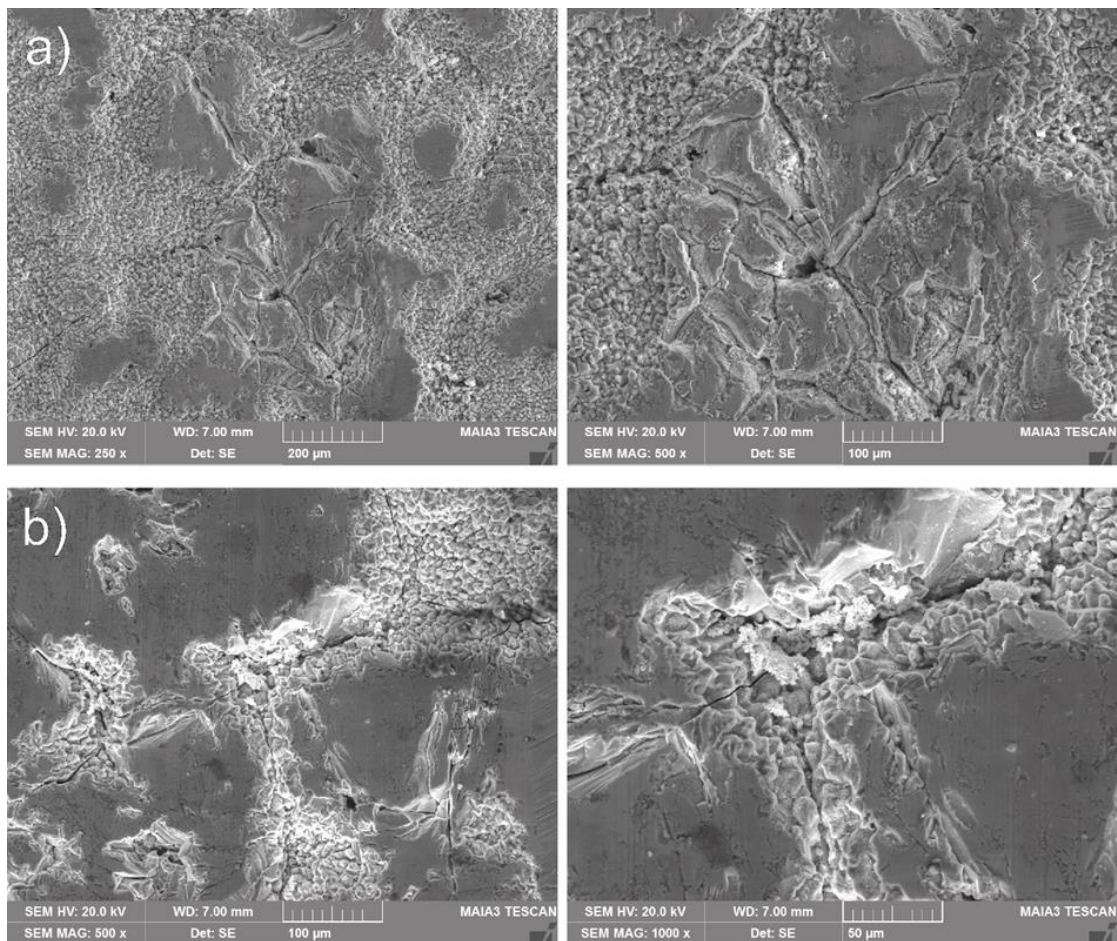


Fig. 15 SEM images of aluminized R4 steel after tribocorrosion test conducted under a) cathodic, b) OCP

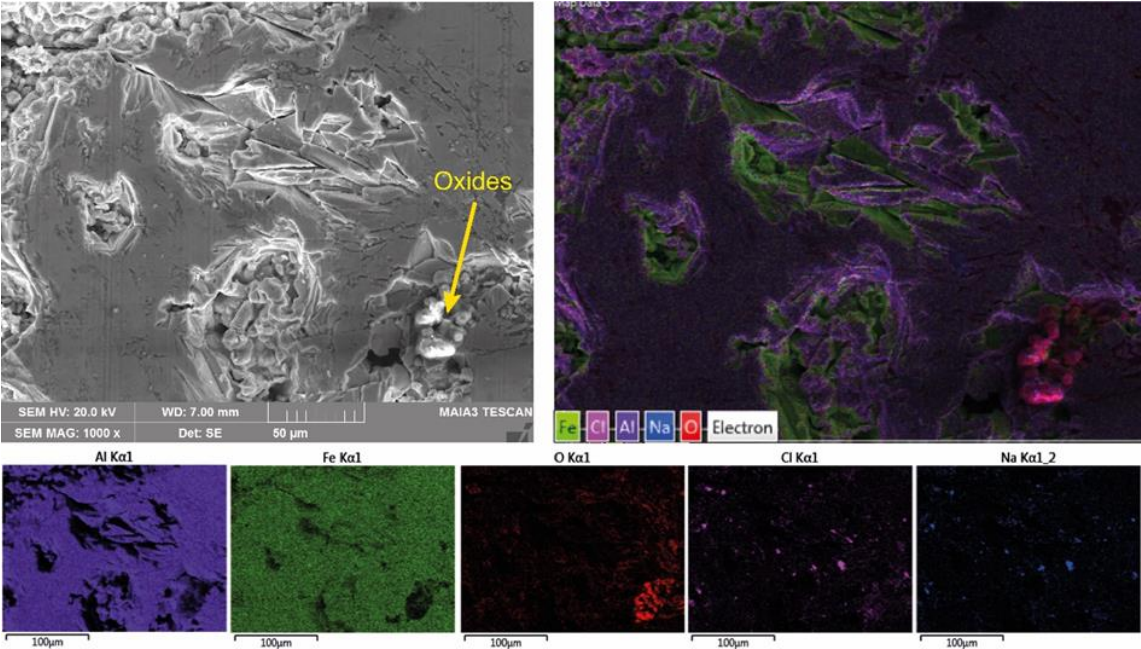


Fig. 16 SEM and EDS images of aluminized R4 steel after tribocorrosion test conducted under OCP

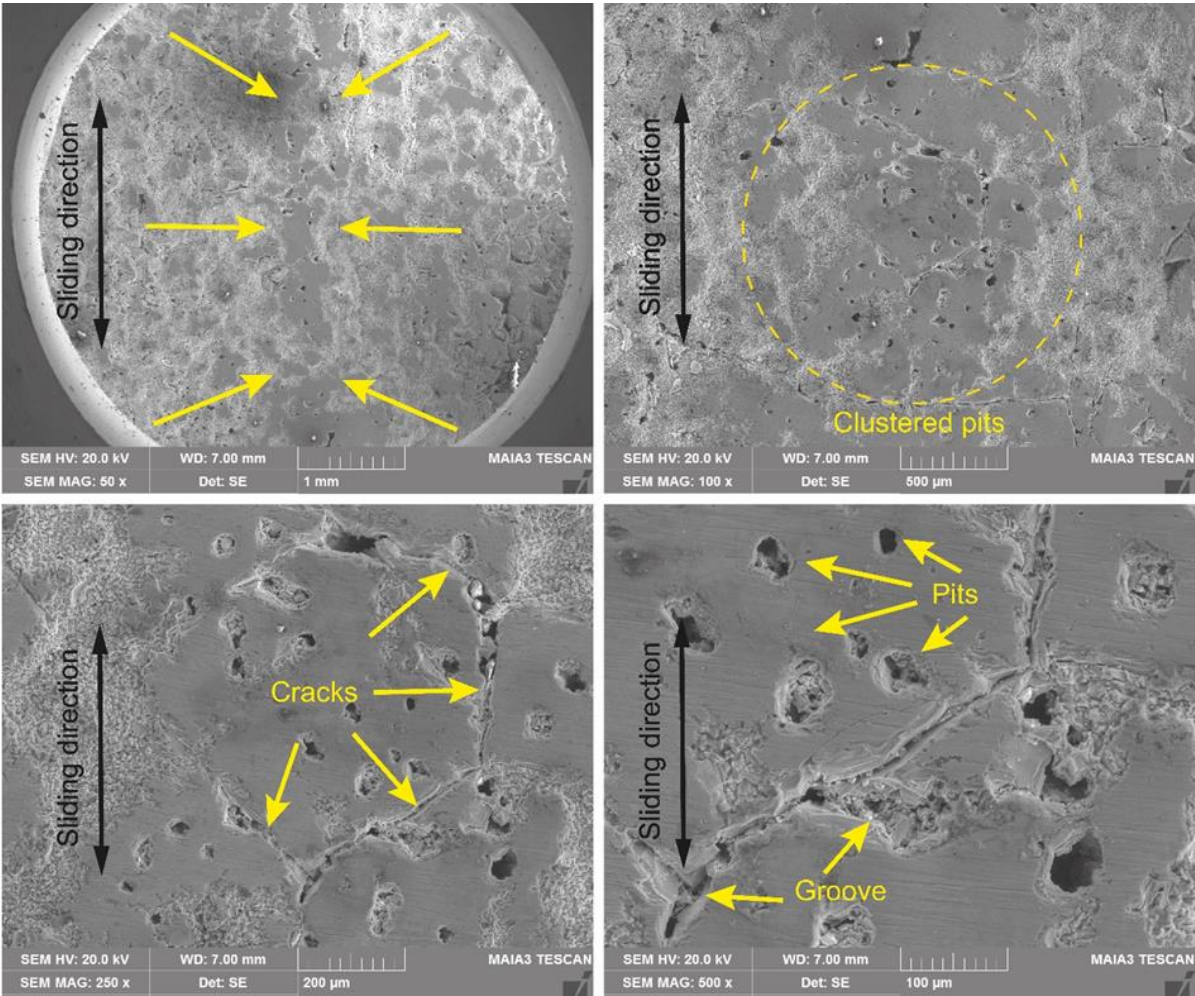


Fig. 17 SEM images of aluminized R4 steel after tribocorrosion test conducted under anodic potential

Fig. 17 represents SEM images of aluminized R4 steel after the tribocorrosion test conducted under anodic potential. The anodic sample also has cracks like cathodic and OCP samples, but the corrosion process was aggressive, and pits were evident in the track. Fig.18 was taken to conduct an EDS analysis. The Cl ions were spread to the whole sample surface, cracks and pits, causing and triggering the pit formation. However, oxides near the cracks prove the anodic dissolution in the wear track.

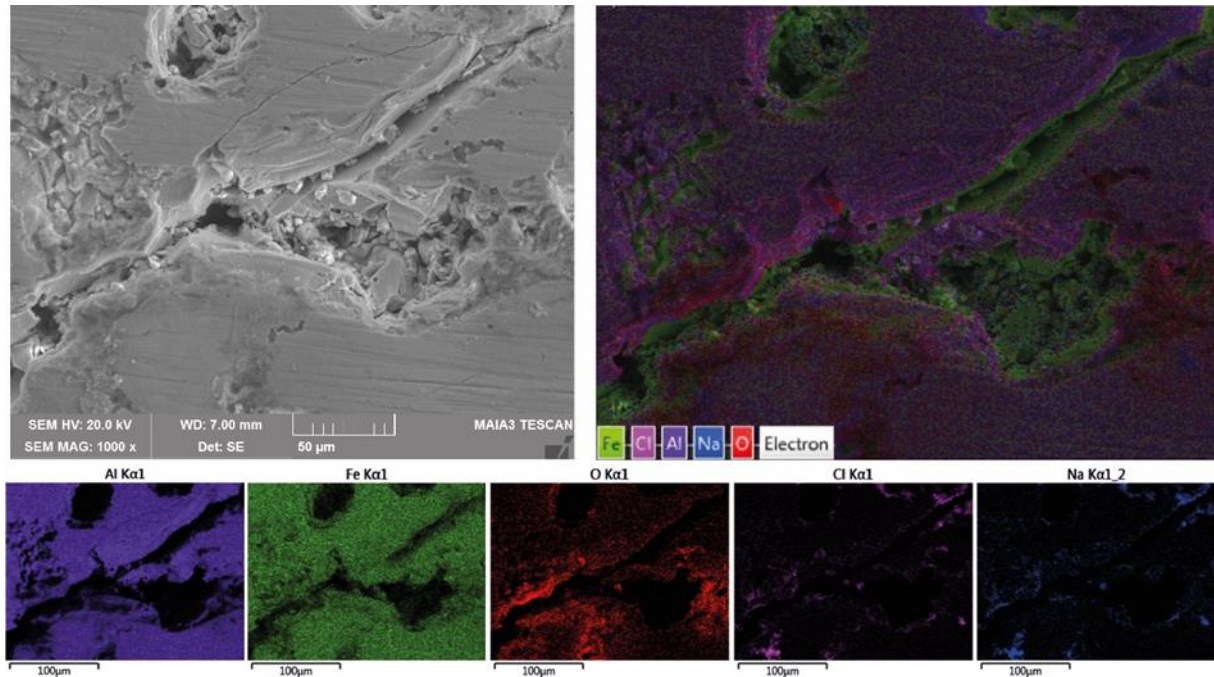


Fig. 18 SEM and EDS images of aluminized R4 steel after tribocorrosion test conducted under anodic potential

3.4 Material loss evaluation

Fig. 19 depicts cross-sections of wear tracks generated under different potentials for R4 and aluminized R4. Superimposed cross sections showed R4 has good wear resistance in NaCl media like other HSLA steels, but according to polarization data, corrosion is the weak side of R4 steel. Although aluminizing process enhanced the corrosion characteristics of R4, it could not decrease material loss from wear track under tribocorrosion conditions. Fig. 20 shows material losses from wear track under different electrochemical conditions. The minor material loss was obtained under cathodic potential in both untreated and aluminized R4, which can be related to pure mechanical wear due to the cathodic protection of samples. More material loss occurred in the aluminized sample under the open circuit potential than in R4. This result was attributed to the wear track of untreated R4 being cathodic while the unworn region was anodic and caused more material loss from the unworn area due to corrosion. This situation is vice-versa for aluminized samples and resulted in more material loss from the wear track and a larger wear track than untreated R4 in all potentials. Also, a sectional view of the pit presented in Fig. 14(c) was inserted in Fig. 19 to show depth and width dimension details under the anodic condition of the aluminide layer. It is nearly 25 μm in depth and 135 μm in width. In the tribocorrosion test performed to understand the behaviour of the prepared aluminium coating layer under anodic conditions, the material loss is considerably higher than in all other cases.

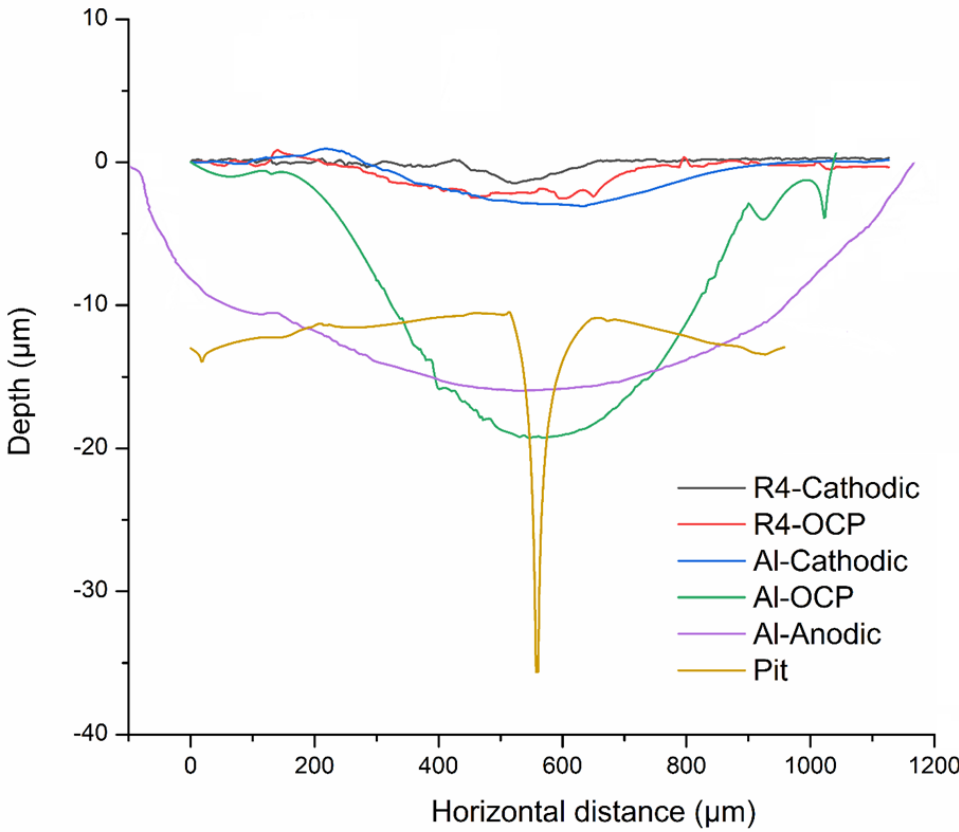


Fig. 19 Cross-sectional profiles of wear tracks and a large pit formed after tribocorrosion tests

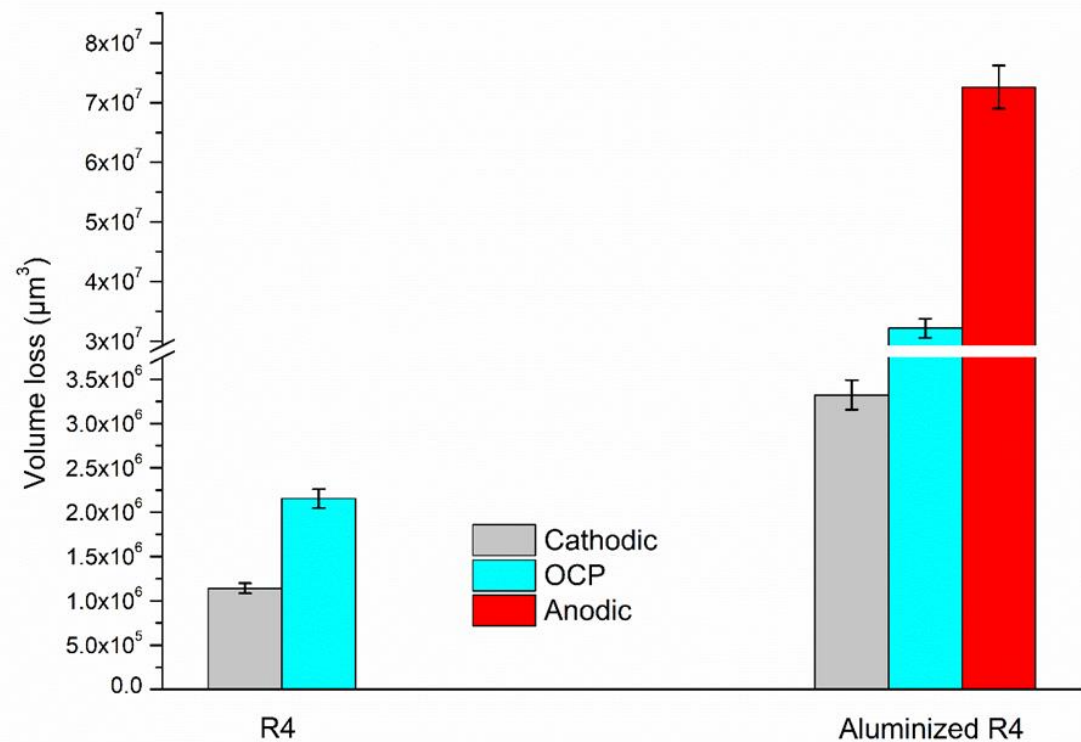


Fig. 20 Material loss volume from wear track under different potentials

4. Conclusions

The present study investigated the effect of the aluminizing process on the corrosion and tribocorrosion behaviour of the R4 grade steel used in offshore mooring line components in 3.5% NaCl. For this purpose, corrosion and linear sliding tribocorrosion tests were carried out on untreated R4 steel substrate and aluminide coating. Finally, the results were compared. From the experimental results, the following conclusions can be drawn:

- An alumina layer consisting of FeAl and Fe₂Al₅ phases with 100 μm thickness and 850HV hardness was obtained on the surface of R4 grade steel. A transition zone with a thickness of 15-20 μm providing high adhesion was achieved between the aluminide layer and the substrate.

- Polarization scans showed significant activation stretch in the current by several orders of magnitude with minor potential variations in the anodic region during corrosion and tribocorrosion in seawater. This result indicates that R4 steel is very active and is highly corroded when immersed in seawater. While untreated R4 steel provided poor corrosion and high corrosion rates, aluminide coating enhanced corrosion resistance with excellent barrier properties.

- The aluminide coating increased corrosion resistance by providing an enhanced tribological response to the steel in simulated seawater. It owes that behaviour to the form oxide layer on the surface, gaining passivation ability with the retarding and blocking effects of the oxide layer.

- During sliding under OCP, the measured current decreased while the potential of the R4 steel increased. This result is attributed to a greater cathodic character inside the track than on the outside due to galvanic effects and the difference in potential, which results in more corrosion in the unworn area for the R4 alloy. The differences in the active and passive character of metals caused the tribocorrosion behaviour for aluminized R4 to occur in the opposite way. In tribocorrosion tests, the corrosion resistance of the steel and the aluminide coating decreased by several orders of magnitude, affected by sliding during the wear process.

- Corrosion products and applied potential strongly affected the friction coefficient of the steel. At the cathodic potential, COF increased due to two hard Al₂O₃ materials and loose metal particles adapting to sliding slip-through cracks on the coating surface, while the lubricating ability of the oxide product film formed at high anodic potential decreased COF. In addition, the pits formed on the wear track at the anodic potential caused a decrease in the contact area, resulting in a reduction in COF.

- SEM and optical microscopy of the R4 steel samples revealed severe abrasion lines in the cathodic and OCP wear track. The corrosion pits were also determined under OCP conditions. On the other hand, a significant amount of corrosion degradation was observed for aluminized R4 at both open circuit and anodic potentials. The tribocorrosion mechanism of the aluminide layer in seawater is a kind of corrosion delamination fatigue, resulting in the micro-fracture of prominent cracks by tribochemical effects.

- The material loss from the wear track increased with the potential increase. For aluminized R4, primary material loss at higher anodic potentials was due to the dissolution of the coating in the wear track rather than the unworn area due to the simultaneous action of wear and corrosion.

While increasing the corrosion resistance of the formed alumina layers, reducing their wear resistance can be attributed to creating a brittle Fe₂Al₅ phase and the ductile FeAl phase in the structure. Therefore, both wear and corrosion resistances can be studied in the future by transforming this phase with secondary heat treatments.

REFERENCES

- [1] Jurišić, P., Parunov, J., Garbatov, Y., 2017. Aging effects on ship structural integrity. *Brodogradnja*, 68(2), 15–28. <https://doi.org/10.21278/brod68202>
- [2] Kim, M. S., Jung, K. H., Park, S. B., 2018. Wave induced coupled motions and structural loads between two offshore floating structures in waves. *Brodogradnja*, 69(3), 149–173. <https://doi.org/10.21278/brod69309>
- [3] Mentés, A., Yetkin, M., 2022. An application of soft computing techniques to predict dynamic behaviour of mooring systems. *Brodogradnja*, 73(2), 121–137. <https://doi.org/10.21278/brod73207>
- [4] Zhang, J., Fowai, I., Sun, K., 2016. A Glance at offshore wind turbine foundation structures. *Brodogradnja*, 67(2), 47–65. <https://doi.org/10.21278/brod67207>
- [5] Farkas, A., Degiuli, N., Martić, I., 2019. Assessment of offshore wave energy potential in the croatian part of the Adriatic sea and comparison with wind energy potential. *Energies*, 12(12), 2357. <https://doi.org/10.3390/en12122357>
- [6] Yeter, B., Garbatov, Y., Guedes Soares, C., 2015. Fatigue damage assessment of fixed offshore wind turbine tripod support structures. *Engineering Structures*, 101, 518–528. <https://doi.org/10.1016/j.engstruct.2015.07.038>
- [7] Kang, J., Sun, L., Sun, H., Wu, C., 2017. Risk assessment of floating offshore wind turbine based on correlation-FMEA. *Ocean Engineering*, 129, 382–388. <https://doi.org/10.1016/j.oceaneng.2016.11.048>
- [8] Li, H., Díaz, H., Guedes Soares, C., 2021. A failure analysis of floating offshore wind turbines using AHP-FMEA methodology. *Ocean Engineering*, 234, 109261. <https://doi.org/10.1016/j.oceaneng.2021.109261>
- [9] Moghaddam, B. T., Hamedany, A. M., Taylor, J., Mehmanparast, A., Brennan, F., Davies, C. M., Nikbin, K., 2020. Structural integrity assessment of floating offshore wind turbine support structures. *Ocean Engineering*, 208, 107487. <https://doi.org/10.1016/j.oceaneng.2020.107487>
- [10] Pham, H. D., Schoefs, F., Cartraud, P., Souldard, T., Pham, H. H., Berhault, C., 2019. Methodology for modeling and service life monitoring of mooring lines of floating wind turbines. *Ocean Engineering*, 193, 106603. <https://doi.org/10.1016/j.oceaneng.2019.106603>
- [11] Ma, K.-T., Luo, Y., Kwan, T., Wu, Y., 2019. Mooring for floating wind turbines. *Mooring System Engineering for Offshore Structures*, 299–315. <https://doi.org/10.1016/B978-0-12-818551-3.00015-6>
- [12] Villa-Caro, R., Carral, J. C., Fraguera, J. Á., López, M., Carral, L., 2018. A review of ship mooring systems. *Brodogradnja*, 69(1), 123–149. <https://doi.org/10.21278/brod69108>
- [13] Barrera, C., Battistella, T., Guanche, R., Losada, I. J., 2020. Mooring system fatigue analysis of a floating offshore wind turbine. *Ocean Engineering*, 195, 106670. <https://doi.org/10.1016/j.oceaneng.2019.106670>
- [14] Brown, M. G., Hall, T. D., Marr, D. G., English, M., Snell, R. O., 2005. Floating production mooring integrity JIP - Key findings. *Proceedings of the Annual Offshore Technology Conference*, 1483–1494. <https://doi.org/10.4043/17499-MS>
- [15] Gordon, R. B., Brown, M. G., Allen, E. M., 2014. Mooring integrity management: A state-of-the-art review. *Proceedings of the Annual Offshore Technology Conference: Proceedings of the Annual Offshore Technology Conference (Vol. 1)*, 577–595. <https://doi.org/10.4043/25134-MS>
- [16] Angulo, Á., Tang, J., Khadimallah, A., Soua, S., Mares, C., Gan, T. H., 2019. Acoustic emission monitoring of fatigue crack growth in mooring chains. *Applied Sciences (Switzerland)*, 9(11), 2187. <https://doi.org/10.3390/app9112187>
- [17] Canut, F. A., Simões, A. M. P., Reis, L., Freitas, M., Bastos, I. N., Castro, F. C., Mamiya, E. N., 2019. Monitoring of corrosion-fatigue degradation of grade R4 steel using an electrochemical-mechanical combined approach. *Fatigue and Fracture of Engineering Materials and Structures*, 42(11), 2509–2519. <https://doi.org/10.1111/ffe.13079>
- [18] Bergara, A., Arredondo, A., Altuzarra, J., Martínez-Esnaola, J. M., 2020. Calculation of stress intensity factors in offshore mooring chains. *Ocean Engineering*, 214, 107762. <https://doi.org/10.1016/j.oceaneng.2020.107762>
- [19] Zhang, X., Hoogeland, M., 2019. Influence of deformation on corrosion of mooring chain steel in seawater. *Materials and Corrosion*, 70(6), 962–972. <https://doi.org/10.1002/maco.201810766>
- [20] Lotfollahi Yaghin, A., Melchers, R. E., 2015. Long-term inter-link wear of model mooring chains. *Marine Structures*, 44, 61–84. <https://doi.org/10.1016/j.marstruc.2015.08.001>

- [21] Argouarc'h, Y., Creac'hedec, R., 2022. Registration method for the analysis of mooring chain links degraded by corrosion and wear. *Ocean Engineering*, 250, 110877. <https://doi.org/10.1016/j.oceaneng.2022.110877>
- [22] Takeuchi, T., Utsunomiya, T., Gotoh, K., Sato, I., 2021. Development of interlink wear estimation method for mooring chain of floating structures: Validation and new approach using three-dimensional contact response. *Marine Structures*, 77(1), 102927. <https://doi.org/10.1016/j.marstruc.2020.102927>
- [23] Noble Denton Europe Limited., 2006. Floating production system: JIP FPS mooring integrity (Research Report No, 2006).
- [24] Lone, E. N., Sauder, T., Larsen, K., Leira, B. J., 2022. Probabilistic fatigue model for design and life extension of mooring chains, including mean load and corrosion effects. *Ocean Engineering*, 245, 110396. <https://doi.org/10.1016/j.oceaneng.2021.110396>
- [25] Nevshupa, R., Martinez, I., Ramos, S., Arredondo, A., 2018. The effect of environmental variables on early corrosion of high-strength low-alloy mooring steel immersed in seawater. *Marine Structures*, 60(3), 226–240. <https://doi.org/10.1016/j.marstruc.2018.04.003>
- [26] Ma, K. T., Shu, H., Smedley, P., L'Hostis, D., Duggal, A., 2013. A Historical Review on Integrity Issues of Permanent Mooring Systems. *Offshore Technology Conference: Offshore Technology Conference (Vol. 3)*. <https://doi.org/10.4043/24025-MS>
- [27] López-Ortega, A., Bayón, R., Arana, J. L., Arredondo, A., Igartua, A., 2018. Influence of temperature on the corrosion and tribocorrosion behaviour of High-Strength Low-Alloy steels used in offshore applications. *Tribology International*, 121, 341–352. <https://doi.org/10.1016/j.triboint.2018.01.049>
- [28] Yeter, B., Garbatov, Y., Guedes Soares, C., 2015. Fatigue damage assessment of fixed offshore wind turbine tripod support structures. *Engineering Structures*, 101, 518–528. <https://doi.org/10.1016/j.engstruct.2015.07.038>
- [29] Wu, J., Tan, F., Zhang, D., Yin, J., Li, E., 2019. Corrosion of Copper-bearing High Strength Mooring Chain Steel Affected by Microbes in Seawater. *Protection of Metals and Physical Chemistry of Surfaces*, 55(6), 1207–1216. <https://doi.org/10.1134/S2070205119060327>
- [30] Von der Ohe, C. B., Johnsen, R., Espallargas, N., 2011. A multi-degradation test rig for studying the synergy effects of tribocorrosion interacting with 4-point static and cyclic bending. *Wear*, 271(11–12), 2978–2990. <https://doi.org/10.1016/j.wear.2011.07.002>
- [31] Ma, K.-T., Luo, Y., Kwan, T., Wu, Y., 2019. Mooring reliability. *Mooring System Engineering for Offshore Structures*, 255–279. <https://doi.org/10.1016/B978-0-12-818551-3.00013-2>
- [32] IACS 2013. Unified IACS Requirements Concerning Materials and Welding – W22 Offshore Mooring Chain. DNV-OS-E30(1993), 28.
- [33] DNV GL 2017. Offshore Standard - Position mooring (DNVGL-OS-E301), Edition July 2017.
- [34] Ivošević, Š., Kovač, N., Momčilović, N., Vukelić, G., 2021. Analysis of corrosion depth percentage on the inner bottom plates of aging bulk carriers with an aim to optimize corrosion margin, *Brodogradnja*. 72(3), 81–95. <https://doi.org/10.21278/brod72306>
- [35] Tezdogan, T., Demirel, Y. K., 2014. An overview of marine corrosion protection with regards to cathodic protection and coatings. *Brodogradnja*, 65(2), 49–59.
- [36] Stojanović, I., Farkas, A., Alar, V., Degiuli, N., 2019. Evaluation of the corrosion protection of two underwater coating systems in a simulated marine environment. *Advances in Surface Engineering*, 71(12), 4330–4338. <https://doi.org/10.1007/s11837-019-03669-4>
- [37] López-Ortega, A., Bayón, R., Arana, J. L., 2019. Evaluation of protective coatings for high-corrosivity category atmospheres in offshore applications. *Materials*, 12(8), 1325. <https://doi.org/10.3390/ma12081325>
- [38] López-Ortega, A., Areitioaurtena, O., Alves, S. A., Goitandia, A. M., Elexpe, I., Arana, J. L., Bayón, R., 2019. Development of a superhydrophobic and bactericide organic topcoat to be applied on thermally sprayed aluminum coatings in offshore submerged components. *Progress in Organic Coatings*, 137, 105376. <https://doi.org/10.1016/j.porgcoat.2019.105376>
- [39] López-Ortega, A., Bayón, R., Arana, J. L., 2018. Evaluation of protective coatings for offshore applications. Corrosion and tribocorrosion behavior in synthetic seawater. *Surface and Coatings Technology*, 349, 1083–1097. <https://doi.org/10.1016/j.surfcoat.2018.06.089>
- [40] Shen, Y., Sahoo, P. K., Pan, Y., 2018. A study of composite coatings on 22mncrnimo steel for mooring chain. *Surface Review and Letters*, 25(3), 1850074. <https://doi.org/10.1142/S0218625X18500749>

- [41] López-Ortega, A., Arana, J. L., Rodríguez, E., Bayón, R., 2018. Corrosion, wear and tribocorrosion performance of a thermally sprayed aluminum coating modified by plasma electrolytic oxidation technique for offshore submerged components protection. *Corrosion Science*, 143(7), 258–280. <https://doi.org/10.1016/j.corsci.2018.08.001>
- [42] Pandim, T., Doca, T., Figueiredo, A. R., Pires, F. M. A., 2020. Torsional fretting wear experimental analysis of a R3 offshore steel against a PC/ABS blend. *Tribology International*, 143(7), 106090. <https://doi.org/10.1016/j.triboint.2019.106090>
- [43] Shen, H. P., Cheng, X. Y., Li, H., Zhang, S. Y., Su, L. C., 2016. Effect of Copper Alloy Element on Corrosion Properties of High Strength Mooring Chain Steel. HSLA Steels 2015, *Microalloying 2015 & Offshore Engineering Steels 2015: HSLA Steels 2015, Microalloying 2015 & Offshore Engineering Steels 2015*, 1201–1209. <https://doi.org/10.1002/9781119223399.ch150>
- [44] Ma, F., Gao, Y., Zeng, Z., Liu, E., 2018. Improving the Tribocorrosion Resistance of Monel 400 Alloy by Aluminizing Surface Modification. *Journal of Materials Engineering and Performance*, 27(7), 3439–3448. <https://doi.org/10.1007/s11665-018-3453-0>
- [45] Bulatović, S., Aleksić, V., Milović, L., Zečević, B., 2021. An analysis of impact testing of high strength low-alloy steels used in ship construction. *Brodogradnja*, 72(3), 1–12. <https://doi.org/10.21278/brod72301>
- [46] Kurt, B., Günen, A., Kanca, Y., Koç, V., Gök, M. S., Kırar, E., Askerov, K., 2018. Properties and tribologic behavior of titanium carbide coatings on AISI D2 steel deposited by thermoreactive diffusion. *Jom*, 70(11), 2650–2659. <https://doi.org/10.1007/s11837-018-3108-5>
- [47] Czerwinski, F. 2012. Thermochemical Treatment of Metals. *Heat Treatment–Conventional and Novel Applications*, 5, 73–112. <https://doi.org/10.5772/51566>
- [48] Günen, A., Kalkandelen, M., Karahan, I. H., Kurt, B., Kanca, E., Gök, M. S., Karakaş, M. S., 2020. Properties and corrosion behavior of chromium and vanadium carbide composite coatings produced on ductile cast iron by thermoreactive diffusion technique. *Journal of Engineering Materials and Technology, Transactions of the ASME*, 142(4). <https://doi.org/10.1115/1.4047743>
- [49] Mittemeijer, E. J., Somers, M. A. J., 2015. Thermochemical Surface Engineering of Steels (Vol. 31). <https://doi.org/10.1080/02670844.2015.1119485>
- [50] Arai, T., 2015. The thermo-reactive deposition and diffusion process for coating steels to improve wear resistance. *Thermochemical Surface Engineering of Steels: Improving Materials Performance*, 703–735. <https://doi.org/10.1533/9780857096524.5.703>
- [51] Günen, A., Soylu, B., Karakaş, Ö., 2022. Titanium carbide coating to improve surface characteristic, wear and corrosion resistance of spheroidal graphite cast irons. *Surface and Coatings Technology*, 437, 128280. <https://doi.org/10.1016/j.surfcoat.2022.128280>
- [52] Yener, T., Doleker, K. M., Erdogan, A., 2019. High temperature oxidation behavior of low temperature aluminized Mirrax® ESR steel. *Materials Research Express*, 6(11), 116407. <https://doi.org/10.1088/2053-1591/ab4541>
- [53] Yener, T., Doleker, K. M., Erdogan, A., Oge, M., Er, Y., Karaoglanli, A. C., Zeytin, S., 2022. Wear and oxidation performances of low temperature aluminized IN600. *Surface and Coatings Technology*, 436(2), 128295. <https://doi.org/10.1016/j.surfcoat.2022.128295>
- [54] Erdogan, A., Yener, T., Doleker, K. M., Korkmaz, M. E., Gök, M. S., 2021. Low-temperature aluminizing influence on degradation of nimonic 80A surface: Microstructure, wear and high temperature oxidation behaviors. *Surfaces and Interfaces*, 25, 101240. <https://doi.org/10.1016/j.surfin.2021.101240>
- [55] Zhan, Z., Liu, Z., Liu, J., Li, L., Li, Z., Liao, P., 2010. Microstructure and high-temperature corrosion behaviors of aluminide coatings by low-temperature pack aluminizing process. *Applied Surface Science*, 256(12), 3874–3879. <https://doi.org/10.1016/j.apsusc.2010.01.043>
- [56] Döleker, K. M., Erdogan, A., Yener, T., Karaoglanlı, A. C., Uzun, O., Gök, M. S., Zeytin, S., 2021. Enhancing the wear and oxidation behaviors of the Inconel 718 by low temperature aluminizing. *Surface and Coatings Technology*, 412, 127069. <https://doi.org/10.1016/j.surfcoat.2021.127069>
- [57] Cardil, A., Monedero, S., Schag, G., Tapia, M. 2021. Microstructure and performance properties of 1200 °C-servicing gradiently aluminized NiCrAlYSi coating for single-crystal nickel-based superalloy. *Journal of Alloys and Compounds*, 924, 165187. <https://doi.org/10.1016/j.jallcom.2022.166619>
- [58] Mariani, F. E., Rêgo, G. C., Bonella, P. G., Neto, A. L., Totten, G. E., Casteletti, L. C., 2020. Wear resistance of niobium carbide layers produced on gray cast iron by thermoreactive treatments. *Journal of Materials Engineering and Performance*, 29(6), 3516–3522. <https://doi.org/10.1007/s11665-020-04645-9>

- [59] Zhang, J., Li, S., Lu, C., Sun, C., Pu, S., Xue, Q., Lin, Y., Huang, M., 2019. Anti-wear titanium carbide coating on low-carbon steel by thermo-reactive diffusion. *Surface and Coatings Technology*, 364(1), 265–272. <https://doi.org/10.1016/j.surfcoat.2019.02.085>
- [60] Mariani, F. E., Takeya, G. S., Lombardi, A. N., Picone, C. A., Casteletti, L. C., 2020. Wear and corrosion resistance of Nb-V carbide layers produced in vermicular cast iron using TRD treatments. *Surface and Coatings Technology*, 397(6), 126050. <https://doi.org/10.1016/j.surfcoat.2020.126050>
- [61] Sun, Y., Dong, J., Zhao, P., Dou, B., 2017. Formation and phase transformation of aluminide coating prepared by low-temperature aluminizing process. *Surface and Coatings Technology*, 330(7), 234–240. <https://doi.org/10.1016/j.surfcoat.2017.10.025>
- [62] Savaş, A., 2021. Selection of welding conditions for minimizing the residual stresses and deformations during hard-facing of mild steel. *Brodogradnja*, 72(1) 1–18. <https://doi.org/10.21278/brod72101>
- [63] Günen, A., 2020. Properties and corrosion resistance of borided AISI H11 tool steel. *Journal of Engineering Materials and Technology*. *Journal of Engineering Materials and Technology*, 142(1), 011010. <https://doi.org/10.1115/1.4044667>
- [64] Günen, A., Kanca, Y., Karahan, İ. H., Karakaş, M. S., Gök, M. S., Kanca, E., Çürük, A., 2018. A comparative study on the effects of different thermochemical coating techniques on corrosion resistance of STKM-13A Steel. *Metallurgical and Materials Transactions A: Physical Metallurgy and Materials Science*, 49(11), 5833–5847. <https://doi.org/10.1007/s11661-018-4862-2>
- [65] Emre, Ö., Mert, D. K., 2021. 904L Paslanmaz çeliğe düşük sıcaklık alüminyumlamının etkisi. *European Journal of Science and Technology*, 28, 1102–1106. <https://doi.org/10.31590/ejosat.1012930>
- [66] Massalski, T. B., Okamoto, H., Subramanian, Kacprzak, L., 2016. Binary Alloy Phase Diagrams. ASM International.
- [67] Yener, T., 2019. Low temperature aluminising of Fe-Cr-Ni super alloy by pack cementation. *Vacuum*, 162(12), 114–120. <https://doi.org/10.1016/j.vacuum.2019.01.040>
- [68] Wang, L., Feng, T., Yu, S., Cheng, Y., Bu, Z., Hu, X., 2019. Fluoride effect on plasma electrolytic oxidation coating formed on Mg-Al alloy in alkaline electrolytes. *Materials Research Express*, 7(1), 016412. <https://doi.org/10.1088/2053-1591/ab60a7>
- [69] Alkan, S., Gök, M. S., 2020. Effect of sliding wear and electrochemical potential on tribocorrosion behaviour of AISI 316 stainless steel in seawater. *Engineering Science and Technology, an International Journal*, 24(2), 524-532.. <https://doi.org/10.1016/j.jestch.2020.07.004>
- [70] López, A., Bayón, R., Pagano, F., Igartua, A., Arredondo, A., Arana, J. L., González, J. J., 2015. Tribocorrosion behaviour of mooring high strength low alloy steels in synthetic seawater. *Wear*, 338, 1–10. <https://doi.org/10.1016/j.wear.2015.05.004>
- [71] Alkan, S., Gök, M. S., 2022. Influence of plasma nitriding pre-treatment on the corrosion and tribocorrosion behaviours of PVD CrN, TiN and AlTiN coated AISI 4140 steel in seawater. *Lubrication Science*, 34(2), 67–83. <https://doi.org/10.1002/ls.1572>
- [72] Alkan, S., 2022. Evaluation of pitting susceptibility and tribocorrosion behaviors of AISI 304 stainless steel in marine environments. *Proceedings of the Institution of Mechanical Engineers, Part J: Journal of Engineering Tribology*. <https://doi.org/10.1177/13506501221113182>
- [73] López-Ortega, A., Arana, J. L., Bayón, R., 2020. On the comparison of the tribocorrosion behavior of passive and non-passivating materials and assessment of the influence of agitation. *Wear*, 456–457(2). <https://doi.org/10.1016/j.wear.2020.203388>
- [74] Çakir, M. V., 2022. A Comparative Study on Tribocorrosion Wear Behavior of Boride and Vanadium Carbide Coatings Produced by TRD on AISI D2 Steel. *Protection of Metals and Physical Chemistry of Surfaces*, 58(3), 562-573. <https://doi.org/10.1134/S2070205122030042>
- [75] Karakaş, M. S., 2020. Tribocorrosion behavior of surface-modified AISI D2 steel. *Surface and Coatings Technology*, 394(5), 125884. <https://doi.org/10.1016/j.surfcoat.2020.125884>
- [76] Günen, A., Ulutan, M., Gök, M., Kurt, B., Orhan, N., 2014. Friction and wear behaviour of borided AISI 304 stainless steel with nano particle and micro particle size of boriding agents. *Journal of the Balkan Tribological Association*, 20(3), 362–379.
- [77] Wong, H. C., Umehara, N., Nato, K. N., 1995. Fundamental study of water-lubricated ceramic bearings. *Transactions of the Japan Society of Mechanical Engineers*, 61, 4073–4032. <https://doi.org/10.1299/kikaic.61.4027>
- [78] Erdogan, A., 2019. Boriding Temperature Effect on Micro-Abrasion Wear Resistance of Borided Tool Steel. *Journal of Tribology*, 141(12), 121702. <https://doi.org/10.1115/1.4044859>

- [79] Günen, A., 2016. Micro-abrasion wear behavior of thermal-spray-coated steel tooth drill bits. *Acta Physica Polonica A*, 130(1), 217–222. <https://doi.org/10.12693/APhysPolA.130.217>
- [80] Marques, F., Da Silva, W. M., Pardal, J. M., Tavares, S. S. M., Scandian, C., 2011. Influence of heat treatments on the micro-abrasion wear resistance of a superduplex stainless steel. *Wear*, 271(9–10), 1288–1294. <https://doi.org/10.1016/j.wear.2010.12.087>
- [81] Zhan, Z., Liu, Z., Liu, J., Li, L., Li, Z., Liao, P., 2010. Microstructure and high-temperature corrosion behaviors of aluminide coatings by low-temperature pack aluminizing process. *Applied Surface Science*, 256(12), 3874–3879. <https://doi.org/10.1016/j.apsusc.2010.01.043>
- [82] Hu, T. L., Huang, H. L., Gan, D., Lee, T. Y., 2006. The microstructure of aluminized type 310 stainless steel. *Surface and Coatings Technology*, 201(6), 3502–3509. <https://doi.org/10.1016/j.surfcoat.2006.07.254>

Submitted: 17.08.2022. Sabri Alkan, salkan@bandirma.edu.tr
Maritime Vocational School of Higher Education, Bandırma Onyedi Eylül
Accepted: 13.11.2022. University, Turkey